J. Fluid Mech. (2022), *vol*. 946, A12, doi:10.1017/jfm.2022.591

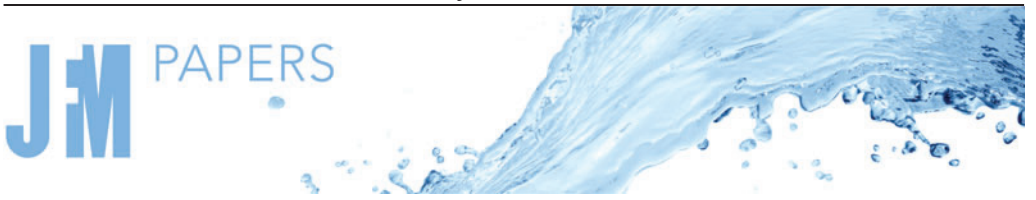

Chordwise flexible aft-tail suppresses jet-switching by reinstating wake periodicity in a flapping foil

Chhote Lal Shah[1], Dipanjan Majumdar[1], Chandan Bose[2] and Sunetra Sarkar[1,3,†]

[1]Department of Aerospace Engineering, IIT Madras, Chennai 600036, India

[2]Department of Aerospace and Mechanical Engineering, University of Liège, Liège 4000, Belgium

[3]Complex Systems and Dynamics Group, IIT Madras, Chennai 600036, India

(Received 6 July 2021; revised 18 June 2022; accepted 28 June 2022)

The effect of a chordwise flexible aft-tail of a rigid heaving aerofoil on the dynamical transitions of the trailing-wake is studied here. The two-way coupled fluid–solid dynamics is simulated using an in-house fluid–structure interaction (FSI) platform, comprising a discrete forcing immersed boundary method based incompressible Navier–Stokes solver, weakly coupled with a finite difference method based structural solver. The FSI dynamics is studied in comparison to the corresponding rigid tail configuration. For the latter, mild jet-switching due to quasi-periodic movement of the wake vortices gives way to vigorous jet-switching as the dynamics transitions to a state of intermittency, where the quasi-periodic behaviour gets interspersed with chaotic windows. Introduction of a moderately flexible tail regularises this intermittent dynamics, eliminating jet-switching. The wake exhibits a deflected reverse Kármán pattern with fluctuating angles, governed by quasi-periodicity. With a highly flexible tail (very low rigidity), the wake shows almost a symmetric reverse Kármán street as periodicity is restored. Flexibility of the aft-tail is next controlled by changing its length, and flow is regularised and periodicity retained for moderate rigidity for increased length. Different dynamical states are established through robust nonlinear dynamical tools. The underlying flow-field behaviour, instrumental in suppressing the jet-switching phenomenon, is identified through a detailed investigation of the near-field vortex interactions dictated by the dynamics. A suite of measures has also been derived from the unsteady flow field to quantify the interactions of the key near-field vortices with a view to understanding the mechanism of switching and its subsequent suppression through flexibility.

Key words: flow-structure interactions

† Email address for correspondence: sunetra.sarkar@gmail.com

1. Introduction

Natural flyers and swimmers exhibit innovative flapping manoeuvres by exploiting the flexibility of their wings or fins in order to maximise the aerodynamic forces. These biological motions have significant potential to be mimicked and adapted in the design of bio-inspired miniature surveillance devices, such as micro aerial vehicles (MAVs) and autonomous underwater vehicles (AUVs). An appropriate understanding of the underlying flow physics is essential to achieve an efficient design. Studies on rigid flapping systems for different kinematics have already established that the key to optimal load generation lies in the ensuing vortex-dominated unsteady flow field surrounding them (Shyy, Berg & Ljungqvist 1999; Triantafyllou, Triantafyllou & Yue 2000; Triantafyllou, Techet & Hover 2004; Shyy *et al.* 2010). Most of the flapping appendages (wings and fins) of biological flyers and swimmers typically possess both spanwise and chordwise flexibility of various degrees, and accordingly their deformation happens during flapping (Ennos 1988; Wootton 1999; Daniel & Combes 2002; Combes & Daniel 2003). Both experimental and numerical studies have demonstrated that elastic deformation of wings/fins has significant impact on their aerodynamic performances (Heathcote & Gursul 2007*a*; Heathcote, Wang & Gursul 2008; Vanella *et al.* 2009; Mazaheri & Ebrahimi 2010; Kang *et al.* 2011; Ramananarivo, Godoy-Diana & Thiria 2011). Results of rigid foils with a deformable tail at a certain flexibility level showing an enhanced efficiency of net power extraction through increased lift generation were presented by Heathcote & Gursul (2007*a*), Ramananarivo *et al.* (2011) and Wu *et al.* (2015).

The existing literature so far has focused mainly on investigating the effects of flexibility from the purview of aerodynamic loads and propulsive efficiency. Despite the knowledge that flexibility may play a key role in achieving efficient flapping flights, the associated flow-field interaction mechanisms are not very clear. The role played by the near-field vortices, and the interactions between the unsteady flow and the flexible body, especially need a careful attention. Note that in natural flapping systems, the flexural rigidity in the spanwise direction is orders of magnitude higher than in the chordwise direction (Combes & Daniel 2003), hence the latter is expected to have a more prominent effect on the flow field and the dynamics. The present study investigates the effects of chordwise flexibility in modifying the near-field interactions with associated wake patterns as well as the related nonlinear dynamical states. A rigid flapping foil with a flexible aft-tail configuration has been considered, which provides a combined approach of exploiting the active control of the rigid foil and the passive deformation of the tail. Also, due to the fact that natural flyers often possess a relatively rigid wing root, the chosen configuration can be considered as a canonical model of a flapping system with varying levels of flexibility.

The wake transition behind rigid flapping foils has been studied comprehensively in the recent literature for different kinematics, such as pure heaving (Lai & Platzer 1999; Lewin & Haj-Hariri 2003; Ashraf, Young & Lai 2012; Badrinath, Bose & Sarkar 2017; Majumdar, Bose & Sarkar 2020*a*,*b*) and pure pitching (Koochesfahani 1989; Godoy-Diana, Aider & Wesfreid 2008; Schnipper, Andersen & Bohr 2009; Shinde & Arakeri 2013), as well as simultaneous heaving–pitching (Lentink *et al.* 2010; Bose & Sarkar 2018; Bose, Gupta & Sarkar 2021; Majumdar, Bose & Sarkar 2022). The dynamic plunge velocity (κh) or Strouhal number (St) was used as the control parameter to study the transition; here, $St = 2f_sA/U_\infty$, where A and f_s are the plunge/heave amplitude and frequency, respectively; $h = A/c$ is the non-dimensional heave amplitude; and $\kappa = 2\pi f_s c/U_\infty$ is the reduced frequency, with c being the chord length of the foil. It is well established that the transition from Kármán to reverse Kármán vortex street, with increasing κh or St, is accompanied

closely by drag-to-thrust transition in the wake (Koochesfahani 1989; Jones, Dohring & Platzer 1998; Lai & Platzer 1999). At higher κh or St ranges, deflected jets through a symmetry-breaking bifurcation emerge, which is associated with increased thrust and a non-zero lift (Jones *et al.* 1998; Lai & Platzer 1999; Godoy-Diana *et al.* 2008). Note that in the periodic regime, a deflected jet remains stable as it does not undergo any temporal change in its deflection direction, which is dictated by the starting condition of the aerofoil motion. However, with further increase in κh or St, the periodicity of the wake is lost gradually. A variety of aperiodic states such as quasi-periodicity and intermittency emerge in this regime, through different local bifurcation routes (Badrinath *et al.* 2017; Bose & Sarkar 2018; Majumdar *et al.* 2020*a*; Bose *et al.* 2021). As a result, spontaneous and repeated reversals in the deflection direction of the reverse Kármán street take place with time, a phenomenon known as jet-switching (Jones *et al.* 1998; Heathcote & Gursul 2007*b*; Shinde & Arakeri 2013; Majumdar *et al.* 2020*b*; Bose *et al.* 2021). Majumdar *et al.* (2020*b*) have shown that quasi-periodic movement of shed vortices acts as the primary trigger for facilitating jet-switching behind a purely heaving foil. In this regime, alternate opposite-sense 'vortex pairing' in the near wake was reported to be the underlying mechanism for triggering jet-switching. However, shedding of strong leading-edge vortices (LEVs) did not take place, and any active interactions with the trailing-edge vortices (TEVs) were also not observed. Hence the LEVs did not participate directly in triggering the switching. In contrast, for a simultaneous heaving–pitching aerofoil, the primary LEV was seen to play the key role behind jet-switching (Bose *et al.* 2021). In the quasi-periodic regime ($\kappa h = 1.6$), Bose *et al.* (2021) observed a spatial reversal in the deflection direction from near- to far-wake, resulting in an arc-shaped pattern in the wake. This particular phenomenon occurred in the far-wake region, and was referred to as far-wake switching. This was triggered by a quasi-periodic disturbance travelling from the LEV, and a subsequent breakdown of a secondary vortex street. A complete reversal in the trailing-edge couple's deflection direction was reported by the same authors at $\kappa h = 1.7$, and this was seen to be associated with the dynamical state of intermittency. The LEV played a crucial role behind the intermittent aperiodic interactions in the near field, enabling the dominant trailing-edge couple to reverse its deflection direction completely. Cleaver, Wang & Gursul (2013) conducted experiments with both an NACA0012 aerofoil and a flat plate at Reynolds number 10 000, and found that for 0° angle-of-attack, NACA0012 produces a stable wake, whereas the flat plate exhibits jet-switching. It was reported that the jet-switching was triggered primarily by the LEV shedding. Note that most of the above studies considered rigid foils, and the role of flexibility behind the transitional wake dynamics did not receive any detailed attention in the literature. In light of the above, the present study focuses on exploring the effect of flexibility on the near-field interactions and jet-switching. None of the previous studies have reported the role of the system's flexibility on the inhibition of jet-switching, interlinking it with the nonlinear dynamical signature of the wake.

The chordwise deformation in the wings/fins introduces additional passive pitching, changing the effective angle-of-attack quite significantly. This can alter considerably the transition scenario in the trailing wake. Existing studies that look into the wake-stabilising effects of flexibility are limited, with the notable exceptions of Marais *et al.* (2012) and Shinde & Arakeri (2014). Marais *et al.* (2012) investigated the wake-transition of a chordwise flexible foil due to passive pitching, and showed that flexibility could inhibit the symmetry-breaking of a reverse Kármán wake and neutralise the deflection

of a jet through strong fluid–structure interaction effects. It was also shown that flexibility could delay the onset of deflection by increasing the separation distance between successively shed TEVs. This is experimental evidence in support of the role of flexibility in altering the wake patterns behind a flapping foil. Heathcote & Gursul (2007*a*,*b*) observed experimentally the presence of jet-switching for a heaving rigid teardrop-shaped foil with a chordwise flexible tail in the quiescent flow condition. The authors observed a quasi-periodic switching pattern, in contrast to the aperiodic pattern reported earlier (Jones *et al.* 1998). Heathcote & Gursul (2007*a*,*b*) did not find any important effect of the flexibility on the jet-switching behaviour in the range of flexibility parameters considered in their study. On the other hand, Shinde & Arakeri (2014) showed that in the quiescent flow condition, a flexible tail of appropriate stiffness could suppress jet-switching by generating a narrow jet, whereas a meandering jet was produced in the absence of flexibility. However, the underlying near-field interactions behind the suppression of switching need more attention and are yet to be clearly understood.

The above studies point out that flexibility can play a crucial role in dictating and modifying the qualitative wake patterns. These observations provide an additional motivation to us to revisit our recently observed dynamical transition routes (Badrinath *et al.* 2017; Bose & Sarkar 2018; Majumdar *et al.* 2020*a*; Bose *et al.* 2021) in the light of introducing flexibility. Specifically, the role of a chordwise flexible aft-tail in changing the wake patterns of a heaving foil by affecting the near-field interactions among the primary wake vortices is focused upon. The effect of additional passive pitching of a flexible tail structure on the nonlinear dynamical signature of the wake is also investigated, which has not been reported in the literature to the best of our knowledge. The primary contents of the present study are: (i) studying the role played by a chordwise flexible aft-tail in altering the qualitative patterns of the trailing wake (such as jet-switching) in comparison to a rigid configuration; (ii) investigating the associated underlying nonlinear dynamical states and bifurcations in the flow field; (iii) understanding the role of deformation of the flexible tail in influencing the leading-edge separation behaviour and the subsequent near-field interactions. To achieve these goals, the flow-field transition for a rigid tail configuration with an increasing dynamic plunge velocity (κh) is studied first. Thereafter, the efficacy of a flexible tail in reinstating the periodicity of the wake by eliminating the jet-switching phenomena is analysed by varying the degree of flexibility. The degree of flexibility is changed in terms of the bending rigidity for a fixed aft-tail length, and subsequently, it is changed by altering the length for a fixed bending rigidity. The underlying nonlinear dynamics behind jet-switching and its regularisation is examined thoroughly using robust time series analysis tools. At this stage, the scope of two-dimensional (2-D) studies in relation to realistic three-dimensional (3-D) engineering applications should also be discussed. Deng, Sun & Shao (2015) and Sun, Deng & Shao (2018) presented the boundary of the 2-D to 3-D transition as a function of non-dimensional stroke amplitude and Strouhal number for the rigid flapping aerofoils using Floquet stability analysis. The kinematic parameters for the present study are chosen in such a way that they lie well inside the 2-D regime. Furthermore, the present study considers so-called high-amplitude/low-frequency flapping, which has been shown to possess coherent LEVs intact in 3-D even at high Strouhal numbers, showing good agreement with the 2-D results (Ashraf *et al.* 2012). However, one should be cautious that the 2-D simulations might fail at high Strouhal numbers for the other class of problems (low-amplitude and high-frequency cases), that may encounter significant spanwise perturbation in the wake (Visbal 2009). Also, in

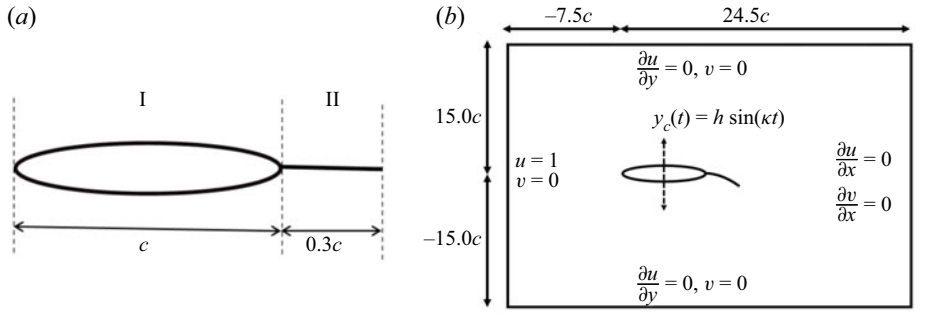

Figure 1. (*a*) A schematic view of the wing configuration; the 'I' and 'II' sections are the rigid foil and flexible tail portions, respectively. (*b*) The computational domain and the boundary conditions (not to scale).

relation to realistic 3-D designs, 2-D results alone may be inadequate for low-aspect-ratio flappers due to the significant tip-vortex effects (Gursul & Cleaver 2019).

The rest of the paper is arranged as follows. In § 2, the structural model and the flow solver are discussed along with convergence tests and validation studies. Section 3 reports the dynamical transition and the presence of the jet-switching phenomenon for the rigid aft-tail configuration. The effect of tail flexibility in altering the same is presented in §§ 4.1 and 4.2. A comparison of the wake for different flexibility levels of the tail in terms of suppression of jet-switching is presented in § 4.3. The effect of the aft-tail length on the flow-field dynamics and its associated mechanism in stabilising the wake is presented in § 4.6. Finally, the salient outcomes of this study and the conclusions are drawn in § 5.

2. Numerical methodology

A rigid elliptic foil of major axis length c, with a chordwise flexible aft-tail of length $0.3c$, is considered to model a 2-D flexible wing configuration, as shown in figure 1(*a*). The thickness to chord ratio of the elliptic section (marked 'I' in figure 1*a*) is 0.12. The Reynolds number is chosen as $Re = 300$. The flow field around the flapping wing is governed by the incompressible Navier–Stokes (N–S) equations. A discrete forcing IBM-based in-house N–S solver is used to simulate the flow field (Majumdar *et al.* 2020*a*). Computationally intensive parts of the flow solver have been parallelised using the OpenMP technique to enhance the computational speed; see Shah, Majumdar & Sarkar (2019). Necessary numerical details of the structural motion, flow solver and fluid–structure coupling are given in the following subsections.

2.1. *Structural governing equations*

A sinusoidal heaving motion: $y_c(t) = h\sin(\kappa t)$ is imposed at the centre of the elliptic foil (figure 1*b*). Here, $y_c(t)$ is the instantaneous position of the centre of a foil in the non-dimensional form, t being the time non-dimensionalised by c/U_∞ (where U_∞ is the free-stream velocity); h and κ denote the non-dimensional heaving amplitude and frequency, respectively. All the quantities throughout this paper are non-dimensionalised, considering c and U_∞ as the reference length and velocity scales, respectively. The flexible tail portion (marked 'II' in figure 1*a*) is modelled as an inextensible filament that is allowed to undergo a passive oscillation. In the non-dimensional form, the governing equation of

the tail motion is given by

$$\beta \frac{\partial^2 \boldsymbol{X}}{\partial t^2} = \frac{\partial}{\partial s}\left(T_s \frac{\partial \boldsymbol{X}}{\partial s}\right) - \frac{\partial^2}{\partial s^2}\left(\gamma \frac{\partial^2 \boldsymbol{X}}{\partial s^2}\right) + \beta\, Fr \frac{\boldsymbol{g}}{g} + \boldsymbol{F}, \tag{2.1}$$

where, s denotes the arc length, $\boldsymbol{X} = (X(s,t), Y(s,t))$ is the position of the filament, T_s is the tension coefficient along the filament, γ is the bending rigidity, and $\boldsymbol{F}$ indicates the fluid force acting on the filament. These non-dimensional quantities are obtained by using characteristic scales $\rho_f U_\infty^2$ for the fluid force, $\rho_f U_\infty^2 c$ for the tension coefficient, and $\rho_f U_\infty^2 c^3$ for the bending rigidity. The mass ratio is defined as $\beta = \rho_s t_h/\rho_f c$, where ρ_s and ρ_f are the solid and fluid densities, respectively; t_h $(= 0.02c)$ is the thickness of the tail structure; $Fr = gc/U_\infty^2$ is the Froude number, with $g = |\boldsymbol{g}|$ being gravitational force. It is to be noted that the gravity term is included here in the structural governing equations alone, solely for the validation of the present solver against the available literature. However, it is not considered for the present fluid–structure interaction (FSI) simulations throughout the study, following the work of Zhu, He & Zhang (2014). In order to maintain a constant length of the tail, the inextensibility condition is implemented as

$$\frac{\partial \boldsymbol{X}}{\partial s} \cdot \frac{\partial \boldsymbol{X}}{\partial s} = 1. \tag{2.2}$$

In (2.1), γ is assumed to be constant. Here, T_s is a function of both s and t, hence T_s is determined by substituting the inextensibility constraint (2.2) in (2.1). This results in a Poisson equation for T_s:

$$\frac{\partial \boldsymbol{X}}{\partial s} \cdot \frac{\partial^2}{\partial s^2}\left(T_s \frac{\partial \boldsymbol{X}}{\partial s}\right) = \frac{\beta}{2}\frac{\partial^2}{\partial t^2}\left(\frac{\partial \boldsymbol{X}}{\partial s} \cdot \frac{\partial \boldsymbol{X}}{\partial s}\right) - \beta \frac{\partial^2 \boldsymbol{X}}{\partial t\, \partial s} \cdot \frac{\partial^2 \boldsymbol{X}}{\partial t\, \partial s} - \frac{\partial \boldsymbol{X}}{\partial s} \cdot \frac{\partial}{\partial s}\left(\boldsymbol{F}_b + \boldsymbol{F}\right), \tag{2.3}$$

where $\boldsymbol{F}_b = -(\partial^2/\partial s^2)(\gamma(\partial^2 \boldsymbol{X}/\partial s^2))$ denotes the bending force. For more details of the formulation of the above equations, one can refer to the work of Huang, Shin & Sung (2007). Note that the non-dimensional reference scales used in this work are different to what was used by Huang *et al.* (2007).

At $t = 0$, the leading edge of the elliptic foil lies at the origin, with the tail at rest in the horizontal position. The boundary conditions for the aft-tail are as follows: at the free end $(s = 1.3c)$,

$$T_s = 0, \quad \frac{\partial^2 \boldsymbol{X}}{\partial s^2} = (0,0), \quad \frac{\partial^3 \boldsymbol{X}}{\partial s^3} = (0,0), \tag{2.4}$$

and at the fixed end $(s = c)$,

$$\boldsymbol{X} = \boldsymbol{X}_0, \quad \frac{\partial \boldsymbol{X}}{\partial s} = (1,0), \tag{2.5}$$

where $\boldsymbol{X}_0 = (c, y_c(t))$ is the position of the leading edge of the aft-tail. Equations (2.1) and (2.3) are solved using a finite difference technique (Huang *et al.* 2007). In order to perform the finite difference discretisation for the structural equations, the flexible filament is divided into N solid elements, each having width Δs and thickness t_h, as shown in figure 2.

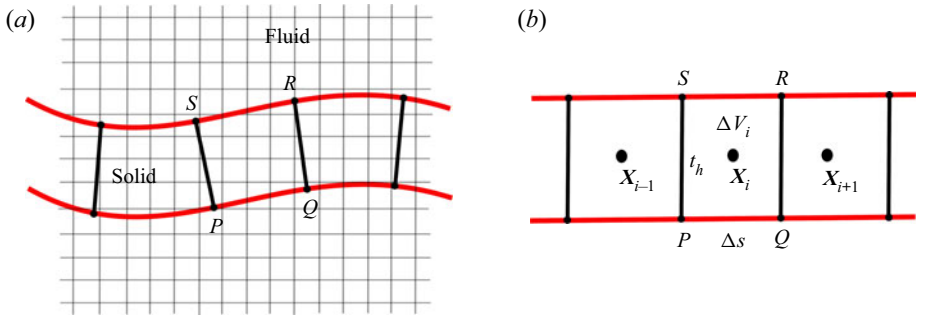

Figure 2. (*a*) Schematic sketch of the flexible filament structure along with the background Eulerian mesh. (*b*) Spatial discretisation strategy of the filament.

2.2. *Flow solver*

In the present IBM solver framework, a momentum forcing $\boldsymbol{f}$ is applied throughout the solid domain to enforce the no-slip, no-penetration boundary condition exactly on the solid boundary (Majumdar *et al.* 2020*a*). In order to ensure rigorous mass conservation across the immersed boundary, a source/sink term q is added to the continuity equation. Hence the flow governing equations take the form

$$\frac{\partial \boldsymbol{u}}{\partial t} + \boldsymbol{\nabla} \cdot (\boldsymbol{uu}) = -\boldsymbol{\nabla} p + \frac{1}{Re} \boldsymbol{\nabla}^2 \boldsymbol{u} + \boldsymbol{f}, \tag{2.6}$$

$$\boldsymbol{\nabla} \cdot \boldsymbol{u} - q = 0. \tag{2.7}$$

Here, $\boldsymbol{u}$ denotes the flow velocity vector non-dimensionalised by U_∞, p is the pressure non-dimensionalised by $\rho_f U_\infty^2$, and the Reynolds number is $Re = U_\infty c/\nu$. Equations (2.6) and (2.7) are solved on a background Eulerian grid using a finite-volume-based semi-implicit fractional step method. The diffusion term is discretised using the second-order Crank–Nicolson method, and Adams–Bashforth discretisation is used for the convection term. At every time step, the velocity is corrected using a pseudo-pressure-correction term. Note that for a grid cell entirely in the fluid domain, which has none of the cell faces inside the solid domain, $\boldsymbol{f}$ and q are considered to be zero. For grid locations inside the solid domain, they take non-zero values. Further details of the flow solver can be found in Kim, Kim & Choi (2001), Lee & Choi (2015) and Majumdar *et al.* (2020*a*).

The fluid force acting on each solid element is calculated using (Lee *et al.* 2011)

$$\boldsymbol{F} = \int_{\Delta V_i} \left(\frac{\partial \boldsymbol{u}}{\partial t} + \boldsymbol{\nabla} \cdot (\boldsymbol{uu}) \right) \mathrm{d}V - \int_{\Delta V_i} \boldsymbol{f} \, \mathrm{d}V, \tag{2.8}$$

where ΔV_i denotes the control volume of each solid element. In figure 2, $\boldsymbol{X}_i$ shows the centre of a typical solid element, and the region bounded by *PQRS* indicates the corresponding control volume. The present formulation requires the size of the Eulerian grid near the solid domain to be much smaller than a solid element, ensuring a sufficient number of fluid cells within a solid element (figure 2*a*), minimising the error involved in computing the volume integrals. The overall lift and drag coefficients, C_L and C_D, respectively, are evaluated by performing the integration given in (2.8) over the entire solid domain. Further details can be found in the studies of Lee & Choi (2015) and Majumdar *et al.* (2020*a*).

The present FSI framework consists of a partitioned weak coupling strategy. In this approach, the flow governing equations are solved to get the flow field around the body at every time step, and the aerodynamic loads acting on the body are evaluated. These loads are then supplied to the structural solver to compute the position/shape of the body for the next time step, and the flow field is then solved with the modified position/shape of the structure. Thus at every time step, the flow and the structural solvers exchange information in a staggered manner.

2.3. *Convergence study*

Schematic representations of the rectangular computational domain and the non-uniform structured Cartesian mesh used in this study are shown in figures 1(*b*) and 3, respectively. The mesh size is uniform in the near-body region and then increases gradually towards the outer boundaries. The size of the flow domain is chosen to be sufficiently large so that the boundary effects are redundant. A Dirichlet-type boundary condition is applied at the inlet, a slip boundary condition is implemented at the upper and lower boundaries, and a Neumann-type boundary condition is employed at the outlet. A total of 1520 Lagrangian markers are used to represent the solid surface. The optimum size of the discretised element for the flexible tail structure to solve the structural equations has been selected after performing a convergence study with the following parametric combination: $h = 0.25$, $\kappa = 4.0$, $\gamma = 0.1$, $\beta = 1.0$, $Fr = 0.0$, $\boldsymbol{g}/g = (0, 0)$ and $Re = 300$. Three different sizes of the structural element, $\Delta s = 0.05, 0.02, 0.005$, have been considered. The structural element length independence test is performed with $\Delta x = \Delta y = 0.005$ and $\Delta t = 0.0004$. The corresponding time histories of the free-end tip deflection of the flexible aft-tail (Y_{te}) are compared in figure 4. The results obtained for $\Delta s = 0.02$ and 0.005 are seen to be in very good agreement with each other. Therefore, the element size for the discretisation of the flexible tail structure is considered to be 0.02 for the rest of the simulations in the present study.

The flow domain is discretised into a mesh consisting of $N_x \times N_y$ grid points, where N_x and N_y indicate the numbers of Cartesian grid points along the streamwise and transverse directions, respectively. Four different meshes, Grid-1, Grid-2, Grid-3 and Grid-4, respectively having minimum grid sizes $\Delta x = \Delta y = 0.01$, $\Delta x = \Delta y = 0.008$, $\Delta x = \Delta y = 0.005$ and $\Delta x = \Delta y = 0.002$, are considered. The corresponding total numbers of grid points $N_x \times N_y$ are 546×748, 614×840, 800×1080 and 1440×1860. The structural element size and time step are kept at $\Delta s = 0.02$ and $\Delta t = 0.0004$, respectively. The aerodynamic load coefficients obtained from these four grids are compared in figure 5. Time evolutions of C_L and C_D obtained from Grid-3 match closely with those obtained from Grid-4. Therefore, Grid-3 is chosen for all further simulations.

To test the time convergence, four different time steps are considered: $\Delta t = 0.001$, 0.0007, 0.0004 and 0.0001 at $\Delta s = 0.02$ and $\Delta x = \Delta y = 0.005$. The corresponding C_L and C_D time histories are compared in figures 6(*a*) and 6(*b*), respectively. The results obtained for $\Delta t = 0.0004$ and 0.0001 are seen to be in very good agreement with each other. Therefore, the time step $\Delta t = 0.0004$ is selected for the rest of the computations.

2.4. *Validation of the FSI solver*

An extensive qualitative and quantitative validation of the flow solver has been presented by the authors in their recent study (Majumdar *et al.* 2020*a*), and therefore is not repeated here for the sake of brevity. Instead, the validation results for the structural response

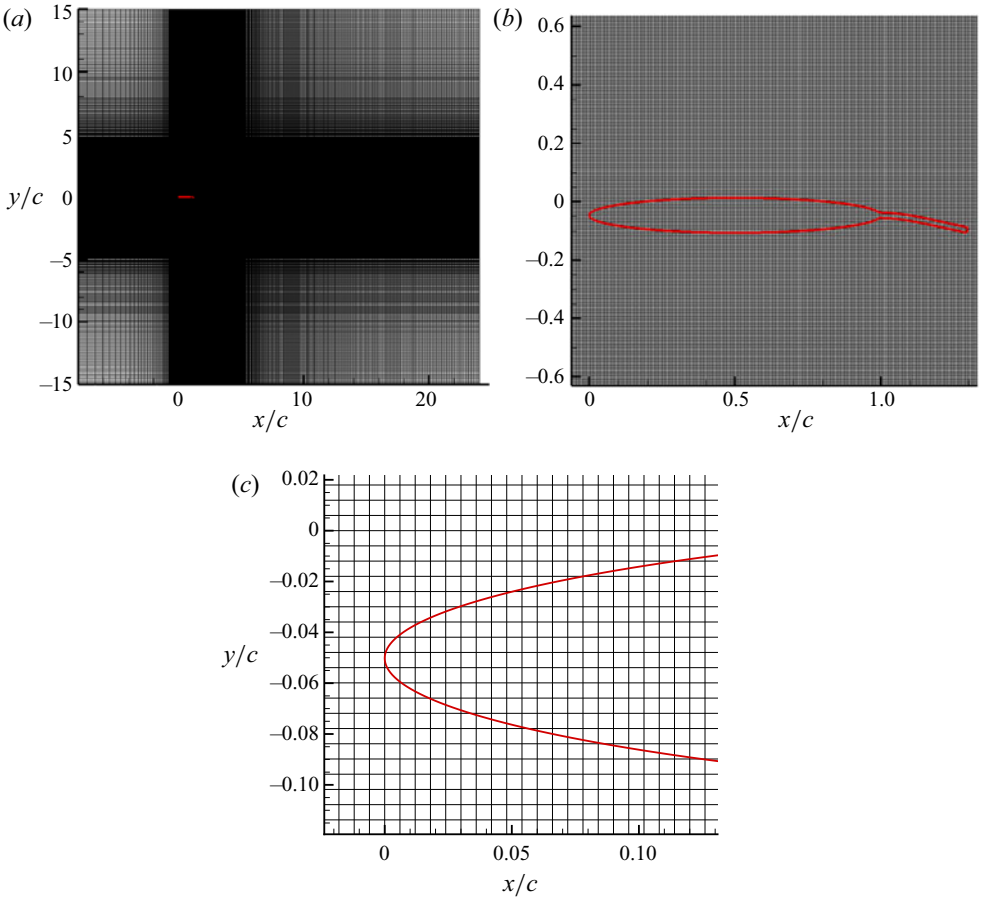

Figure 3. Meshing strategy: (*a*) Cartesian grid, (*b*) zoomed section of the background grid around the foil with a flexible tail, and (*c*) uniform mesh grid near the body.

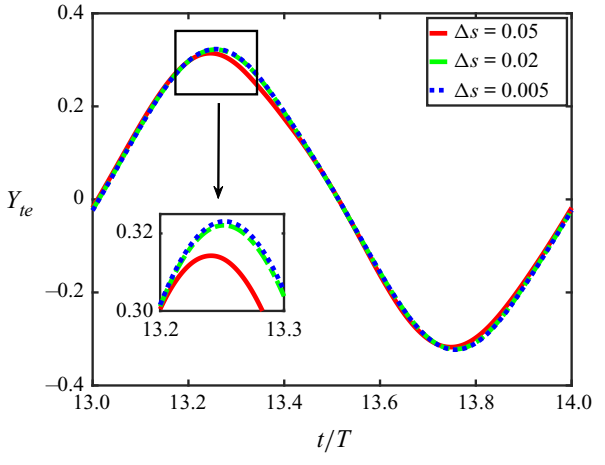

Figure 4. Convergence study for the number of elements considered for the trailing edge.

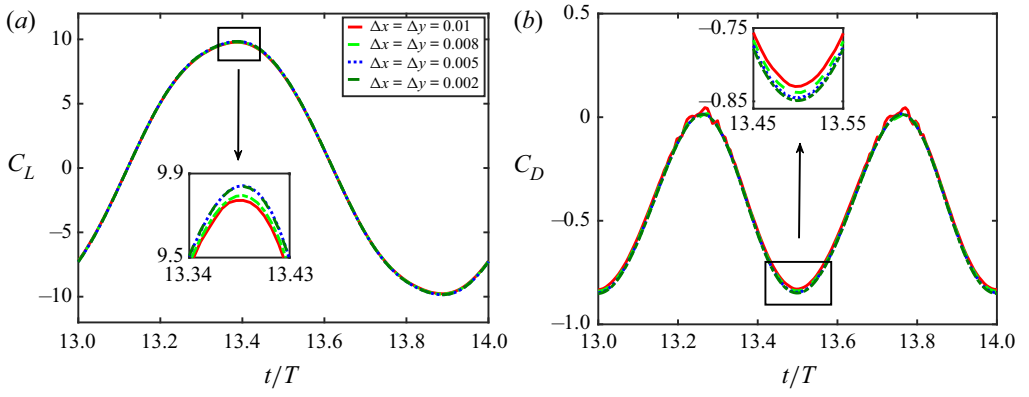

Figure 5. Grid convergence study: (*a*) lift coefficient, and (*b*) drag coefficient.

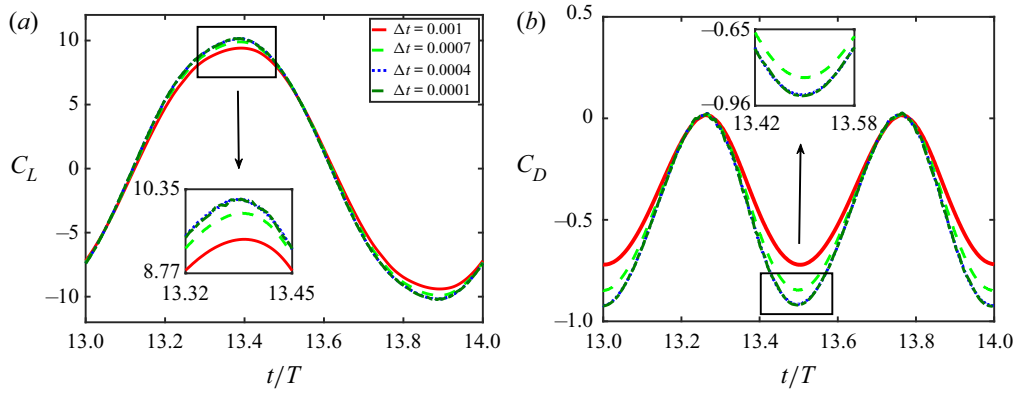

Figure 6. Time step convergence study: (*a*) lift coefficient, and (*b*) drag coefficient.

and the coupled FSI response are presented in two stages: first, the structural solver is validated, and next, the validation of the coupled FSI solver is presented using structural displacement as well as flow-field and aerodynamic loads. For validating the structural solver alone, a flexible filament hanging under the gravitational force is considered in the absence of any ambient fluid. The time history of the free-end displacement of the filament (Y_{te}) obtained from the present solver is compared with the results presented by Huang *et al.* (2007) in figure 7(*a*). A close match between these results confirms the capability of the structural solver.

The coupled FSI solver is validated first by simulating the interaction of a flexible filament with the surrounding free stream at $Re = 200$. Figure 7(*b*) shows a comparison of the time history of Y_{te} obtained from present solver with the results from the works of Huang *et al.* (2007) and Lee & Choi (2015). The C_L and C_D time histories are also compared with the results presented by Lee & Choi (2015) in figures 8(*a*) and 8(*b*), respectively. It is evident from figures 7(*b*) and 8 that the present FSI results are in very good agreement with these earlier published data, establishing the validity of the current FSI solver. A qualitative comparison of the instantaneous flow-field data with that presented by Lee & Choi (2015) is also given in figure 9. A close match between the two further confirms the efficacy of the present in-house FSI solver.

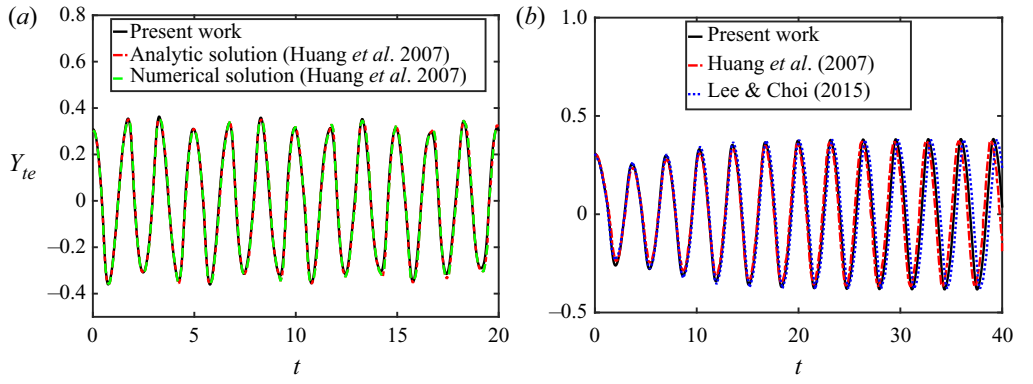

Figure 7. Validation of the present solver set-up in terms of the free-end tip displacement: (*a*) for a flexible filament hanging under the gravitational force in the absence of ambient fluid at $\gamma = 0.01$, $Fr = 10$, $\boldsymbol{g}/g = (1, 0)$, $L = 1$ and $N = 100$; and (*b*) for the FSI behaviour of a flexible filament in the presence of upstream flow at $Re = 200$, $\gamma = 0.0015$, $\beta = 1.5$, $Fr = 0.5$, $\boldsymbol{g}/g = (1, 0)$, $L = 1.0$ and $N = 100$. Parametric symbols follow the definitions given by Huang *et al.* 2007.

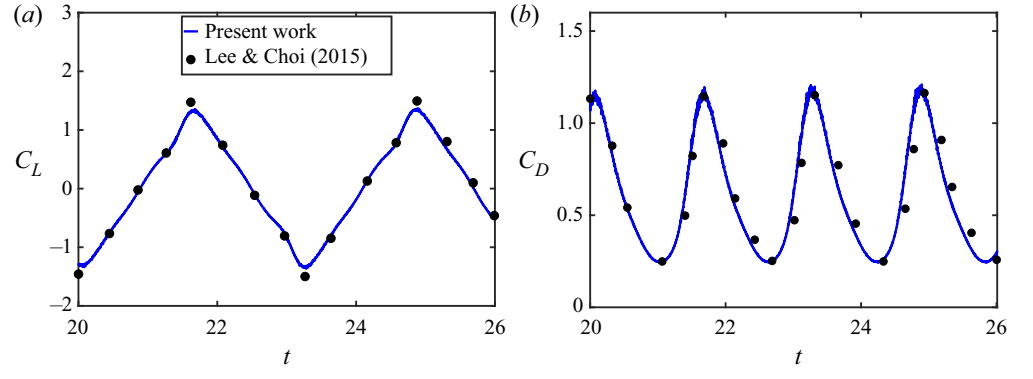

Figure 8. Validation of the present solver set-up in terms of the aerodynamic loads: (*a*) lift coefficient and (*b*) drag coefficient time histories of a flexible filament undergoing FSI with the surrounding free stream at $Re = 200$, $\gamma = 0.0015$, $\beta = 1.5$, $Fr = 0.5$, $\boldsymbol{g}/g = (1, 0)$, $L = 1.0$ and $N = 100$.

To add further quantitative validation, the flow past a NACA0015 aerofoil with a flexible aft-tail, a configuration similar to the present study, is simulated and compared with the computational results of Wu *et al.* (2015). The Reynolds number is $Re = 1100$, and the foil undergoes an active pitching and an induced heaving motion. Results from the present simulations are compared with Wu *et al.* (2015), in terms of instantaneous lift coefficient C_L and its root-mean-square values, $(C_L)_{rms}$, in figures 10(*a*) and 10(*b*), respectively. The present simulations corroborate well with Wu *et al.* (2015), providing further quantitative validation in the concerned Reynolds number regime.

The present solver has also been used to compare with the experimental results of Heathcote & Gursul (2007*b*), where jet-switching was studied in detail. Heathcote & Gursul (2007*b*) considered a rigid teardrop foil with a flexible tail having length of two times the chord of the rigid foil, under quiescent flow conditions. The same configuration with the same level of flexibility has been used in the present validation simulations under quiescent flow conditions. Due to the limitations of the numerical schemes and algorithms used in the current IBM solver, the simulations were run at a lower $Re_f =$

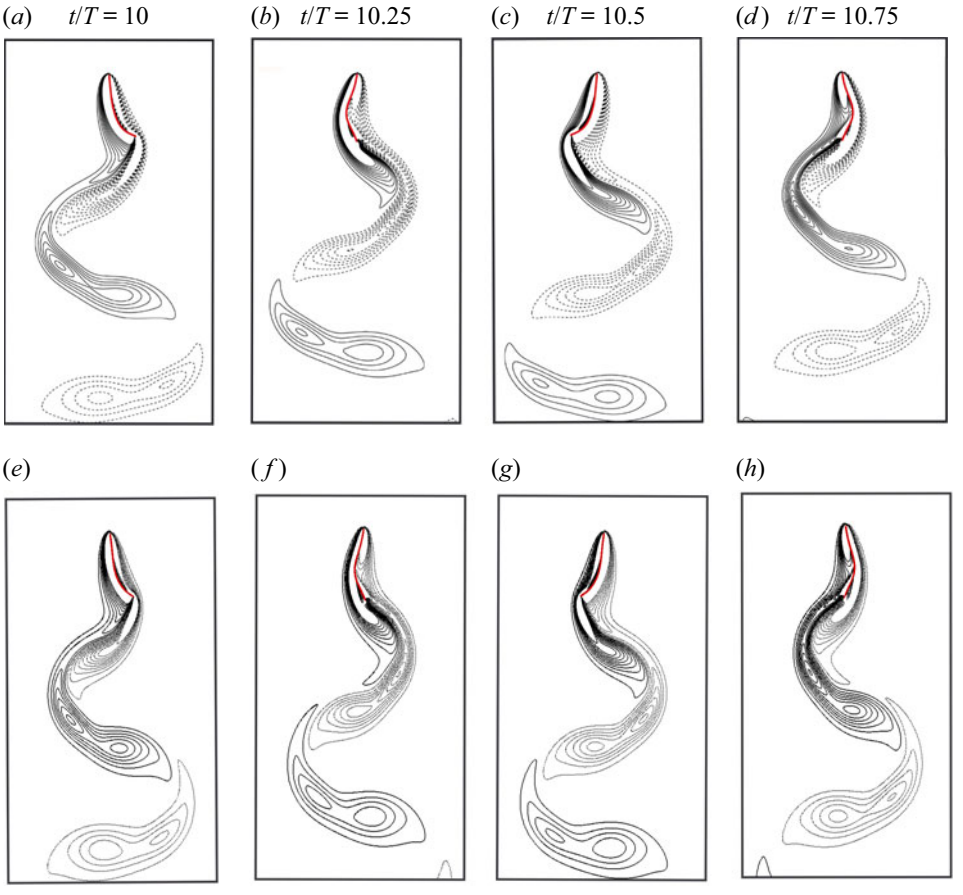

Figure 9. Comparison of vorticity fields between that from Lee & Choi (2015) (*a–d*) and the present simulation (*e–h*) of a flexible filament undergoing FSI with the surrounding free stream at $Re = 200$, $\gamma = 0.0015$, $\beta = 1.5$, $Fr = 0.5$, $\boldsymbol{g}/g = (1, 0)$, $L = 1.0$ and $N = 100$. Permission for reproducing the figures from Lee & Choi (2015) has been obtained from the publisher.

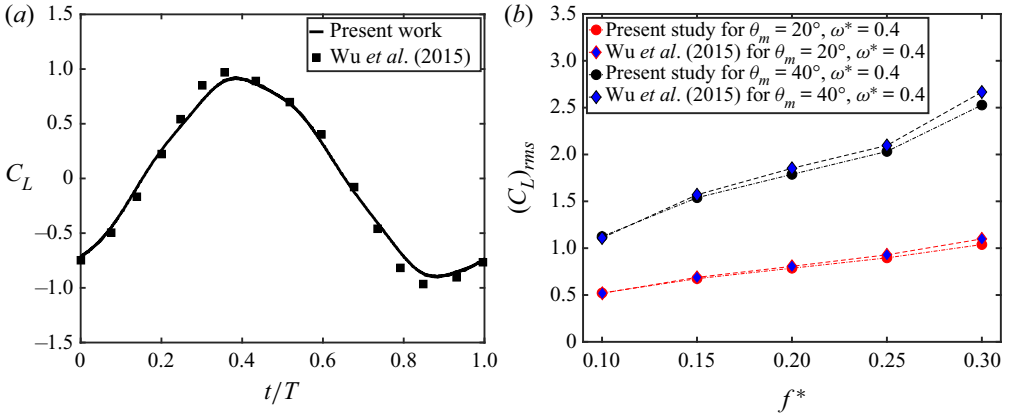

Figure 10. (*a*) Comparison of lift coefficient C_L for $\theta_m = 20°$, $m_t^* = 5$, $\omega^* = 0.4$ and $f^* = 0.15$. (*b*) Root-mean-square values of lift coefficient $(C_L)_{rms}$ with the work of Wu *et al.* (2015) at $Re = 1100$. Parametric symbols follow the definitions given by Wu *et al.* (2015).

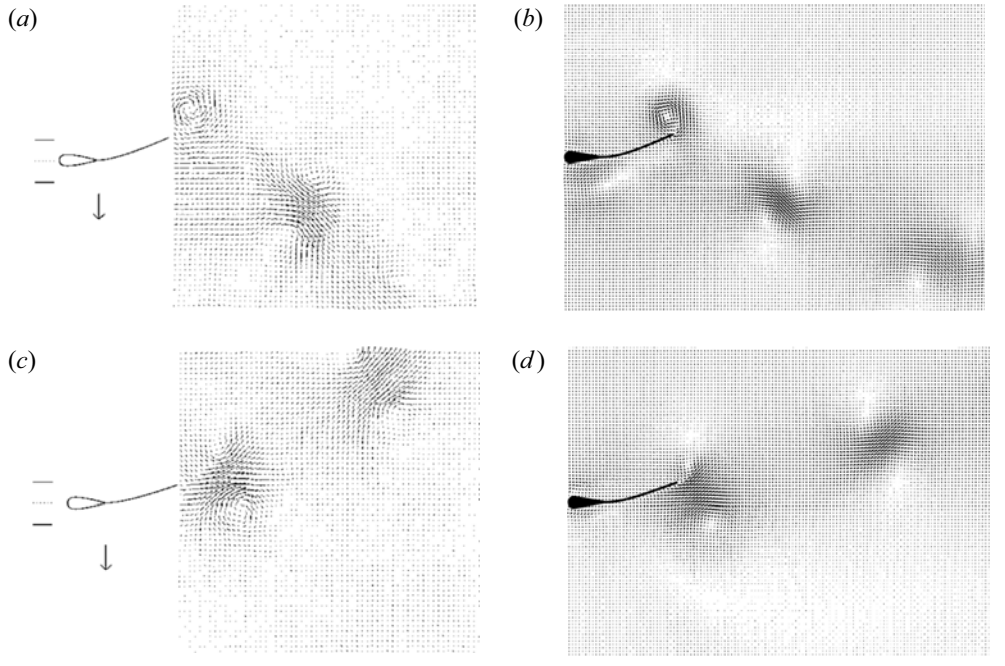

Figure 11. Comparison of the velocity vector field for two representative flapping cycles, showing the jet-switching phenomenon under quiescent flow conditions: (*a*,*c*) experimental results reported by Heathcote & Gursul (2007*b*), and (*b*,*d*) simulation results; $h = 0.194$ and $b/c = 1.13 \times 10^{-3}$. Note that the parametric symbols follow the definitions given by Heathcote & Gursul (2007*b*), equivalent to $\gamma = 0.496$. Permission for reproducing the figures from Heathcote & Gursul (2007*b*) has been obtained from the publisher.

$f_s c^2/\nu = 300$, whereas in the experiments, the value of Re_f was 16 200. This comparison is presented to establish the capability of the FSI solver in capturing the jet-switching phenomenon. Figure 11 shows the qualitative comparison of the wake patterns. It is seen from figures 11(*a*,*c*) and figures 11(*b*,*d*) that the jet-switching phenomenon is captured properly under the quiescent flow. For quantitative comparison, the vortex core locations of the counter-clockwise and clockwise vortices are shown in figures 12(*a*) and 12(*b*) together with the results of Heathcote & Gursul (2007*b*), and an overall agreement is observed in the time window considered. The temporal evolution of the flow field corresponding to figure 11 is presented in supplementary movie 5 available at https://doi.org/10.1017/jfm.2022.591.

3. Flow-field transition in the wake with a rigid aft-tail

The rigid system is considered as the base configuration in this study, and the associated flow field and nonlinear dynamical states are used as a benchmark to compare with the results of the flexible configurations. The rigid case results are presented in this section. In the next section, two different flexible tail configurations with $\gamma = 0.1$ and 0.01 (referred to as flexibility levels I and II, respectively) are discussed. To follow the qualitative changes in the flow field for the case of a rigid aft-tail, κh is varied as the control parameter. The results are presented for three typically chosen parametric values to show the representative wake patterns of importance: three heave amplitudes, $h = 0.25, 0.3, 0.375$, have been considered at a fixed reduced frequency $\kappa = 4.0$, resulting in $\kappa h = 1.0, 1.2, 1.5$. The rigid

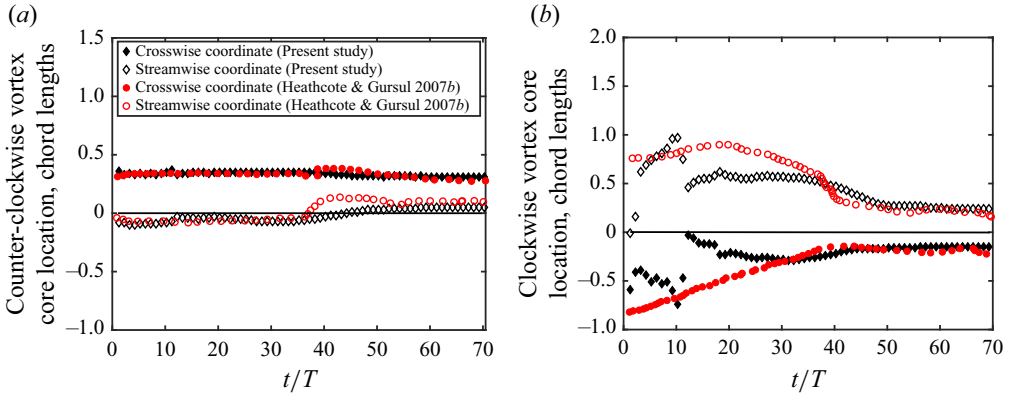

Figure 12. Comparison of vortex core location in chord lengths obtained from the present simulation and the experimental work of Heathcote & Gursul (2007*b*); $h = 0.194$ and $b/c = 1.13 \times 10^{-3}$. Note that the parametric symbols follow the definitions given by Heathcote & Gursul (2007*b*), equivalent to $\gamma = 0.496$: (*a*) counter-clockwise vortex, and (*b*) clockwise vortex.

Parameters	Values
Mass ratio	$\beta = 1.0$
Reynolds number	$Re = 300$
Reduced frequency	$\kappa = 4.0$
Non-dimensional heave amplitude	$h = 0.25, 0.3, 0.375$
Flexibility level I	$\gamma = 0.1$
Flexibility level II	$\gamma = 0.01$

Table 1. Parameter space.

aft-tail configuration represents the limiting case of bending rigidity, $\gamma \to \infty$. The flow Reynolds number is chosen to be constant at $Re = 300$. The other system parameters that remain constant for all the simulations are $\beta = 1.0$, $Fr = 0.0$ and $\boldsymbol{g}/g = (0, 0)$. Table 1 summarises the parameter space considered in the present study. In addition, to understand the effect of the aft-tail length (L_t) in retaining the periodicity in wake and inhibiting jet-switching, L_t is changed by keeping the bending rigidity fixed at $\gamma = 0.1$, and the results are presented for a typical value $L_t = 0.38c$ in this study. For the rigid aft-tail configuration, the flow field exhibits a mildly deflected reverse Kármán wake at $\kappa h = 1.0$, associated with periodic dynamics. At $\kappa h = 1.2$, mild jet-switching is observed in the wake, which turns into vigorous jet-switching involving much higher deflection angles at $\kappa h = 1.5$.

The upward or downward deflection of the trailing wake is characterized based on the overall wake deflection angle Θ (Godoy-Diana *et al.* 2009; Majumdar *et al.* 2020*b*). It is defined as the angle between the mean position of heaving motion (denoted by the dashed-dotted line) and the average wake deflection direction (denoted by the dashed line); see figure 13(*a*). Upward and downward deflected wakes are indicated by the positive and negative values of Θ, respectively. To understand the mechanism of jet-switching, a system of the first three vortices present in the wake at the end of a flapping cycle is considered following the works of Wei & Zheng (2014) and Majumdar *et al.* (2020*b*); see figure 13(*b*). Here, vortices $\boldsymbol{A}$, $\boldsymbol{B}$ and $\boldsymbol{C}$ refer to the first counter-clockwise (CCW), first clockwise (CW)

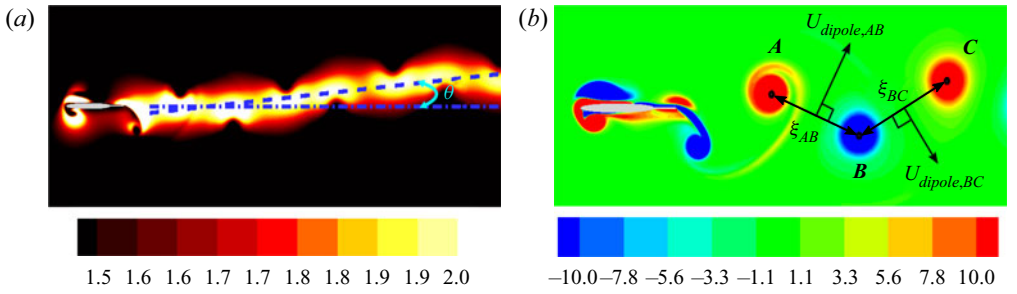

Figure 13. (*a*) Definition of the deflection angle (Θ). (*b*) Schematic representation of the system of the first three vortices in the trailing wake used in the present analysis.

and second CCW vortex, respectively. As the flow evolves, if the distance between vortices ***A*** and ***B*** becomes less than that between ***B*** and ***C***, then vortex couple ***A***–***B*** forms the dominant upward deflecting couple (Majumdar *et al.* 2020*b*). It eventually deflects the entire wake in the upward direction in the subsequent cycles, which is the direction of its self-induced dipole velocity. The opposite scenario takes place during the formation of ***B***–***C***, the dominant downward deflecting couple, which induces the wake to deflect downwards. They will be referred to as 'symmetry-breaking couples' here. Eventually, the mutual competition between these two symmetry-breaking couples dictates the overall deflection direction of the wake (Godoy-Diana *et al.* 2009; Zheng & Wei 2012). The dominance of either ***A***–***B*** or ***B***–***C*** is illustrated here using the ratio of their self-induced dipole velocities. It is defined as U_{dipole}-ratio $= U_{dipole,AB}/U_{dipole,BC}$, where U_{dipole} is the self-induced dipole velocity evaluated as (Anderson 2010)

$$U_{dipole} = \frac{\Gamma_{avg}}{2\pi\xi}. \tag{3.1}$$

Here, ξ denotes the distance between the two partners of a vortex couple, and Γ_{avg} is the average of the absolute circulation values of the two partners. Also, U_{dipole}-ratio can be evaluated as the ratio of two quantities, Γ_{avg}-ratio (defined as $\Gamma_{avg,AB}/\Gamma_{avg,BC}$) and ξ-ratio (defined as ξ_{AB}/ξ_{BC}). Throughout this paper, terms 'AB' or 'BC' added in the suffix of any quantity/measure designate that particular quantity/measure to be associated with couple ***A***–***B*** or ***B***–***C***, respectively. For more discussion on the above-mentioned quantities, please refer to Godoy-Diana *et al.* (2009), Zheng & Wei (2012), Wei & Zheng (2014) and Majumdar *et al.* (2020*b*). The computational methodology for Γ and ξ is depicted in § 1 of the supplementary material for the sake of brevity. The qualitatively different wake behaviours are also associated with different nonlinear dynamical states, as will be established in the following subsections using a series of nonlinear time series analysis tools; the detailed description of these tools can be found in § 2 of the supplementary material and is also available in our earlier studies (Badrinath *et al.* 2017; Bose & Sarkar 2018).

3.1. $\kappa h = 1.0$: *reverse Kármán wake with mild deflection (periodic dynamics)*

At this κh, the trailing wake exhibits a reverse Kármán vortex street with a small downward deflection with $\Theta \approx -0.1^\circ$, as shown in figure 14 in terms of the instantaneous vorticity and velocity magnitude contours. Time variation of Θ is presented in figure 15(*a*). A mild dominance of downward deflecting couple ***B***–***C***, indicated by the U_{dipole}-ratio less than

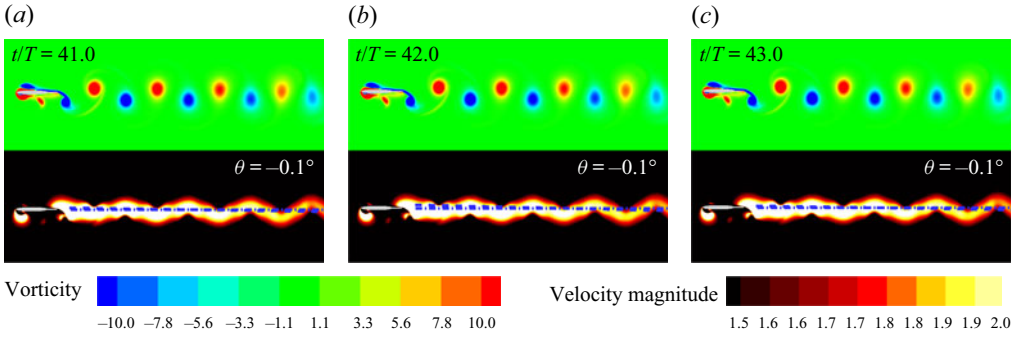

Figure 14. For $\kappa h = 1.0$, rigid tail: instantaneous vorticity (top) and velocity magnitude (bottom) contours depicting a reverse Kármán wake with mild downward deflection. Note that the same contour levels have been used throughout the paper for all the vorticity and velocity contour plots, and are therefore not repeated hereafter.

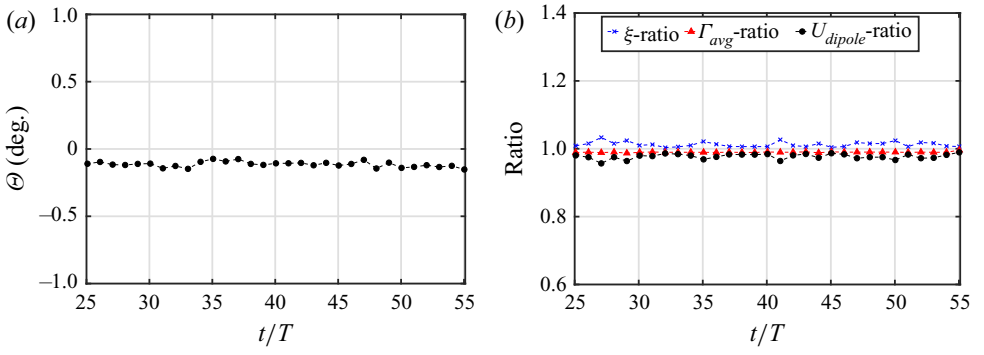

Figure 15. For $\kappa h = 1.0$, rigid tail: (*a*) wake deflection angle, (*b*) quantitative measures associated with the vortex system. Dominant effect of the downward deflecting vortex couple ***B*–*C*** results in negative deflecting angle.

unity (figure 15*b*), is able to direct the wake towards the downward direction. In figure 14, the vortex structures repeat in the consecutive flapping cycles due to the periodic nature of the flow field, resulting in a periodic C_D time history as shown in figure 16(*a*). The closed-loop behaviour of the phase portrait in the reconstructed phase space (figure 16*b*), the dominant frequency peak corresponding to twice the heaving frequency accompanied by super harmonics in the frequency spectra (figure 16*c*), and the wavelet spectra with a narrow frequency band (figure 16*d*), all confirm the periodic dynamics.

Due to flow periodicity, the same vortex couple ***B*–*C*** remains dominant throughout, leading to a downward deflected wake for all time; see figure 15(*a*). The minor variation in the Θ time history can be attributed to the small changes observed in the ξ-ratio, while the Γ_{avg}-ratio remains almost constant; see figure 15(*b*). These results are also quite similar to our earlier results for a rigid heaving system without any aft-tail (Majumdar *et al.* 2020*b*).

3.2. $\kappa h = 1.2$: *mild jet-switching (quasi-periodic dynamics)*

With an increase in κh, the magnitude of the wake deflection angle increases, and a jet-switching behaviour is seen to take place around $\kappa h = 1.2$; see figure 17. Figure 18(*a*)

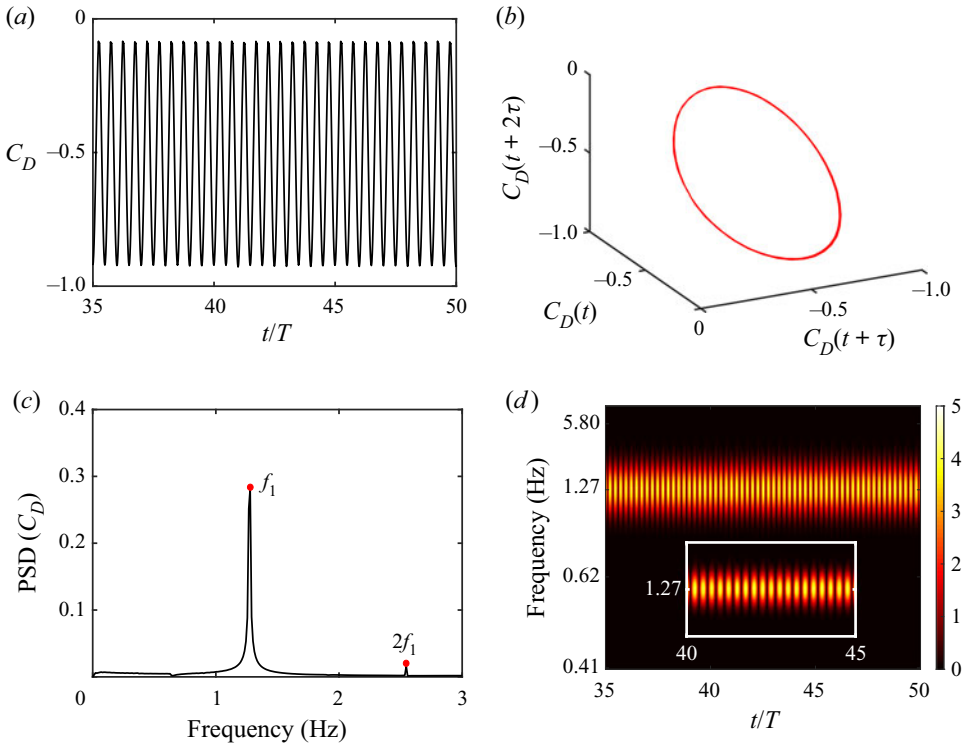

Figure 16. For $\kappa h = 1.0$, rigid tail, time series analysis of C_D indicates periodic dynamics: (*a*) time history, (*b*) reconstructed phase portrait, (*c*) frequency spectra (where PSD denotes power spectral density), and (*d*) wavelet transform.

shows that Θ changes its sign from positive to negative and vice versa, multiple times. The modulating oscillation in the C_D time history (figure 19*a*) represents the quasi-periodic behaviour of the flow field, which can be confirmed from the corresponding reconstructed phase space showing a toroidal portrait; see figure 19(*b*). The presence of quasi-periodicity can be proven further by the frequency spectra, which comprise two incommensurate frequencies, $f_1 = 1.27$ and $f_2 = 0.61$, along with other non-harmonic peaks that are in a linear combination of these two; see figure 19(*c*). These incommensurate frequency bands are also visible in the wavelet spectra (figure 19*d*). The quasi-periodic wake interactions trigger jet-switching by inducing small changes in vortex strengths and vortex core locations in different cycles (Majumdar *et al.* 2020*b*). As a result, the distances between the wake vortices change, leading to alternate dominance of upward and downward deflecting couples through the 'vortex pairing' process. The alternate dominance of the symmetry-breaking couples is depicted in terms of the variation in U_{dipole}-ratio in figure 18(*b*). The dominant symmetry-breaking couple, while convecting downstream, pulls the fluid behind it, forcing the mean jet to deflect in the direction of its self-induced velocity (Godoy-Diana *et al.* 2009). The subsequent vortices follow the path dictated by the dominant couple, resulting in a deflected street. As the relative dominance shifts alternately between the upward deflecting ***A*–*B*** and downward deflecting ***B*–*C***, they force the vortex street to switch the deflection direction alternately.

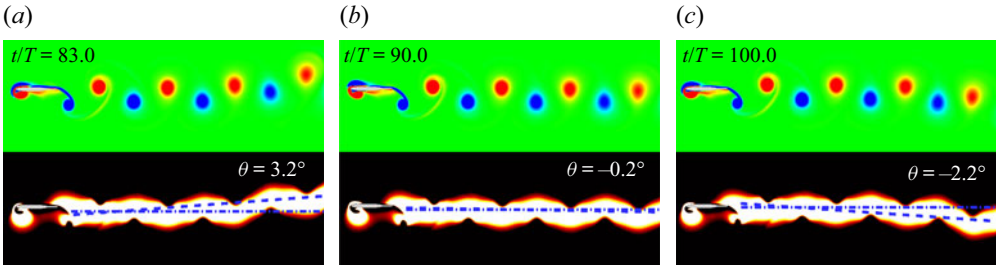

Figure 17. For $\kappa h = 1.2$, rigid tail: instantaneous vorticity (top) and velocity magnitude (bottom) contours showing mild jet-switching.

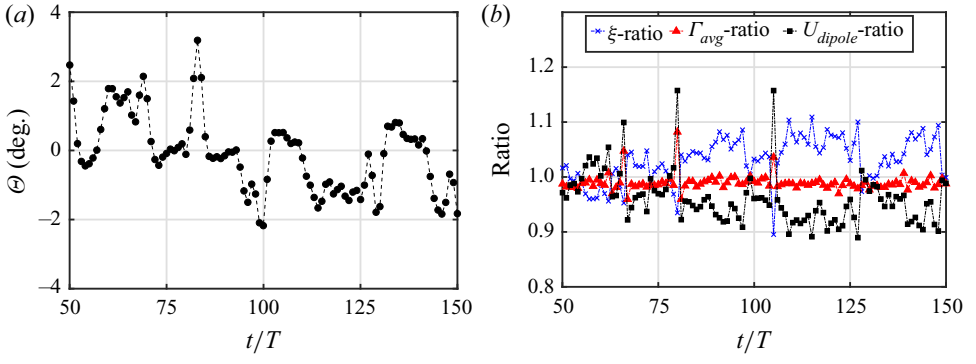

Figure 18. For $\kappa h = 1.2$, rigid tail: (*a*) wake deflection angle, (*b*) quantitative measures associated with the vortex system. Alternate dominance of the upward and downward deflecting vortex couples leads to jet-switching.

3.3. $\kappa h = 1.5$: *prominent jet-switching with higher deflection angles (dynamical state of intermittency)*

As κh is increased further to 1.5, the jet-switching phenomenon becomes more prominent and the vortex street fluctuates with higher deflection angles compared to the previous case; see figure 20. The rapidity of switching also increases notably in this regime. The augmentation of jet-switching is triggered by strong intermittent perturbations from the primary LEV and its subsequent interactions with the TEV (as is discussed later in this subsection). As a result, the quasi-periodic pattern gets intermittently laden with irregular windows of chaotic bursts. In the nonlinear dynamics literature, such temporal patterns in which the system alternates irregularly between the states of quasi-periodicity and chaos are known as type-II intermittency (Hilborn *et al.* 2000). The C_D time history in figure 21(*a*) shows two such typical chaotic windows (marked by rectangular boxes B_1 and B_2) in between the quasi-periodic modulations. Note that the reconstructed phase space (figure 21*b*) and the frequency spectra (figure 21*c*) are unable to capture the properties of these intermittent behaviours, and reflect an average quasi-periodic behaviour instead. However, the temporal evolution of the frequency content presented in the wavelet spectra (figure 21*d*) captures clearly the intermittency behaviour through the sporadic bursts of broadband frequencies. The recurrence plot in figure 22 also identifies the two different dynamical states (quasi-periodic and chaotic) present in the system. The quasi-periodic state is characterised by the unequally spaced lines parallel to the main diagonal, whereas

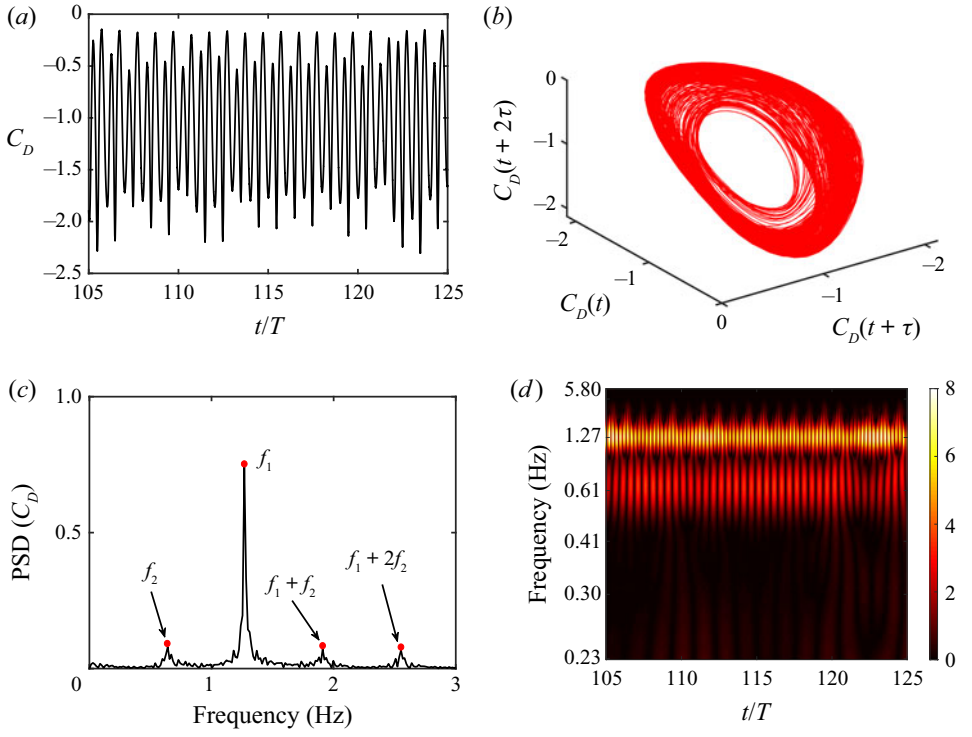

Figure 19. For $\kappa h = 1.2$, rigid tail, time series analysis of C_D indicates quasi-periodic dynamics: (*a*) time history, (*b*) reconstructed phase portrait, (*c*) frequency spectra, and (*d*) wavelet transform.

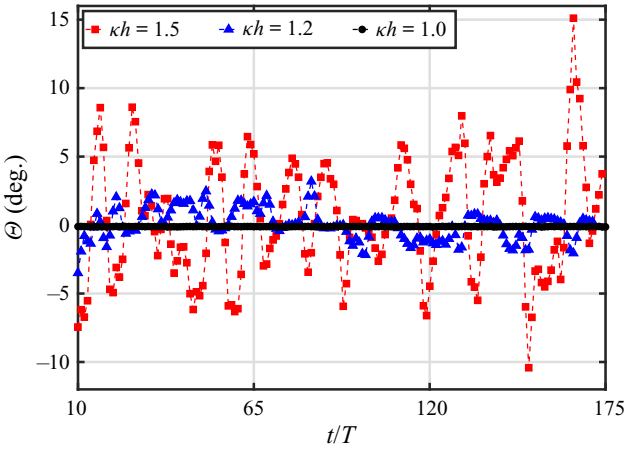

Figure 20. Rigid tail configuration; variation in the wake deflection angle.

the short and broken lines along with isolated points (marked by windows B_1 and B_2 in figure 22) are representative of the chaotic state.

Recall that in the quasi-periodic regime, jet-switching started through the process of alternate dominance of upward and downward deflecting couples. The marginal shifts in the positions of the wake vortices was instrumental in flipping this dominance, and the LEVs had no direct contribution in jet-switching. However, during the state of

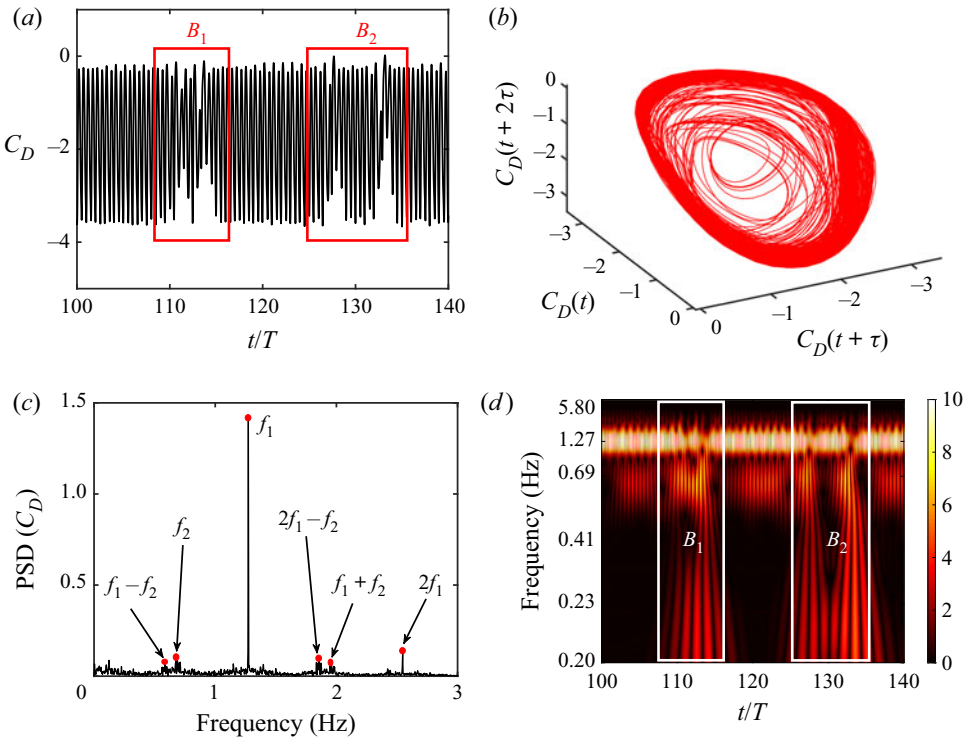

Figure 21. For $\kappa h = 1.5$, rigid tail, time series analysis of C_D during type-II intermittency: (*a*) time history, (*b*) reconstructed phase portrait, (*c*) frequency spectra, and (*d*) wavelet transform.

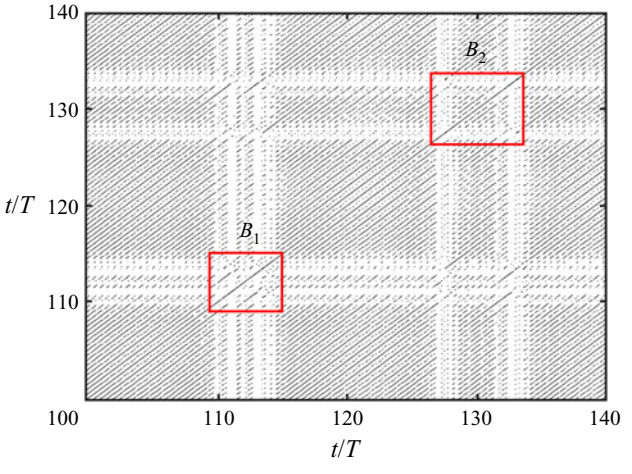

Figure 22. For $\kappa h = 1.5$, rigid tail: recurrence plot of C_D (depicting intermittency).

intermittency, LEVs become important in the switching process through LEV–TEV interactions as the chaotic bursts provide strong perturbations in the near-field region. This results in the formation of strong symmetry-breaking couples at the trailing edge. A similar near-field behaviour was also observed by Bose *et al.* (2021) for a no-tail configuration. For the present case, figure 23 shows the evolution of the primary LEVs (***L*1**–***L*16**) tracked

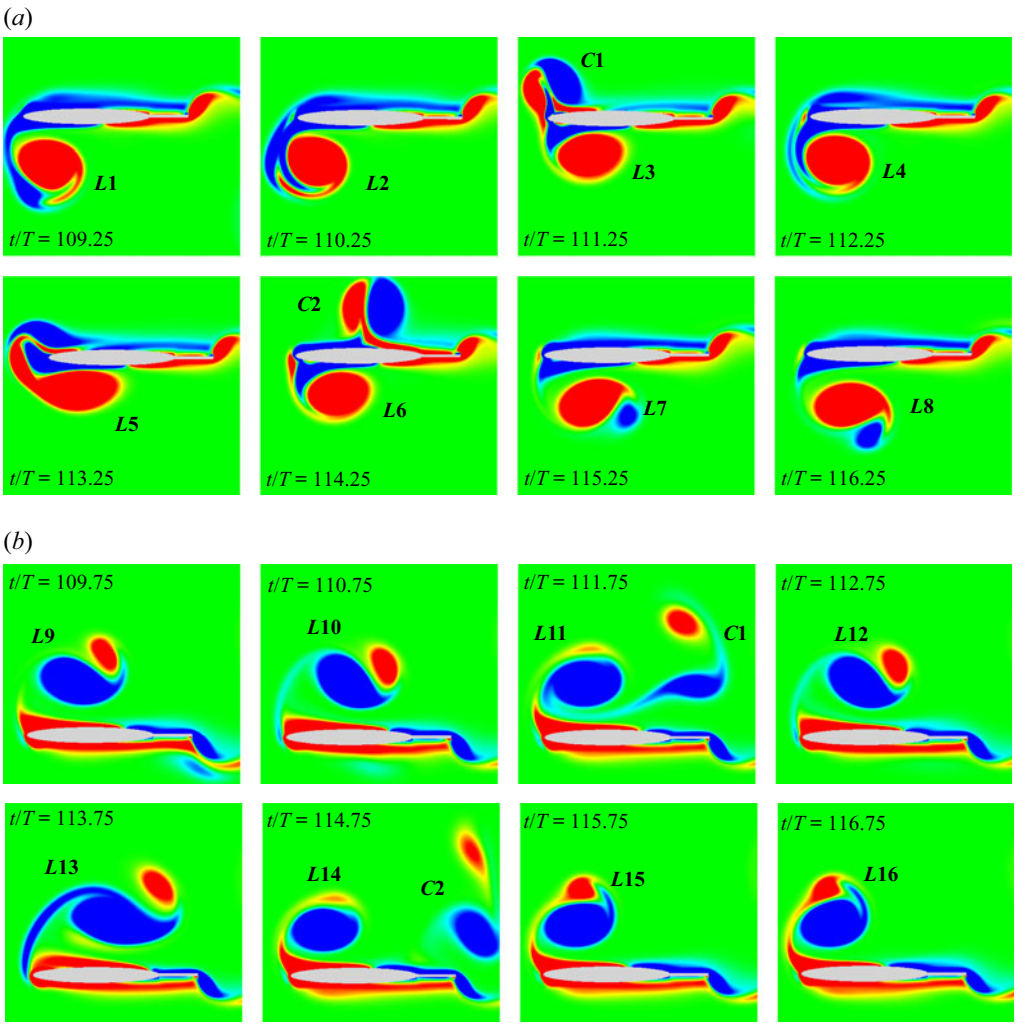

Figure 23. For $\kappa h = 1.5$, rigid tail: LEV behaviour during the aperiodic window B_1 towards the end of (*a*) upstrokes and (*b*) downstrokes.

for eight consecutive flapping cycles during the chaotic window B_1. The snapshots are presented for the same phases of the cycles, and they are chosen during the ends of upstrokes and downstrokes. The primary LEVs are named differently for different flapping cycles in figure 23 as their strengths and locations differ from one cycle to another during the chaotic window. Towards the end of the upstrokes, aperiodic leading-edge separation is observed that leads to shedding of vortex couples of different strengths at different cycles, either from the leading edge (***C1***) or from the mid-surface (***C2***). Shedding of leading-edge couples from the lower surface is hindered during a few cycles by the circumnavigation of another couple on the upper surface (e.g. see ***L5*** at $t/T = 113.25$ in figure 23*a*). This aperiodic growth and convection of the LEVs affect their subsequent interactions with the TEVs considerably.

In order to understand the role of intermittency in enhancing jet-switching, the chronology of vortex interactions from five consecutive cycles (112th to 116th) during

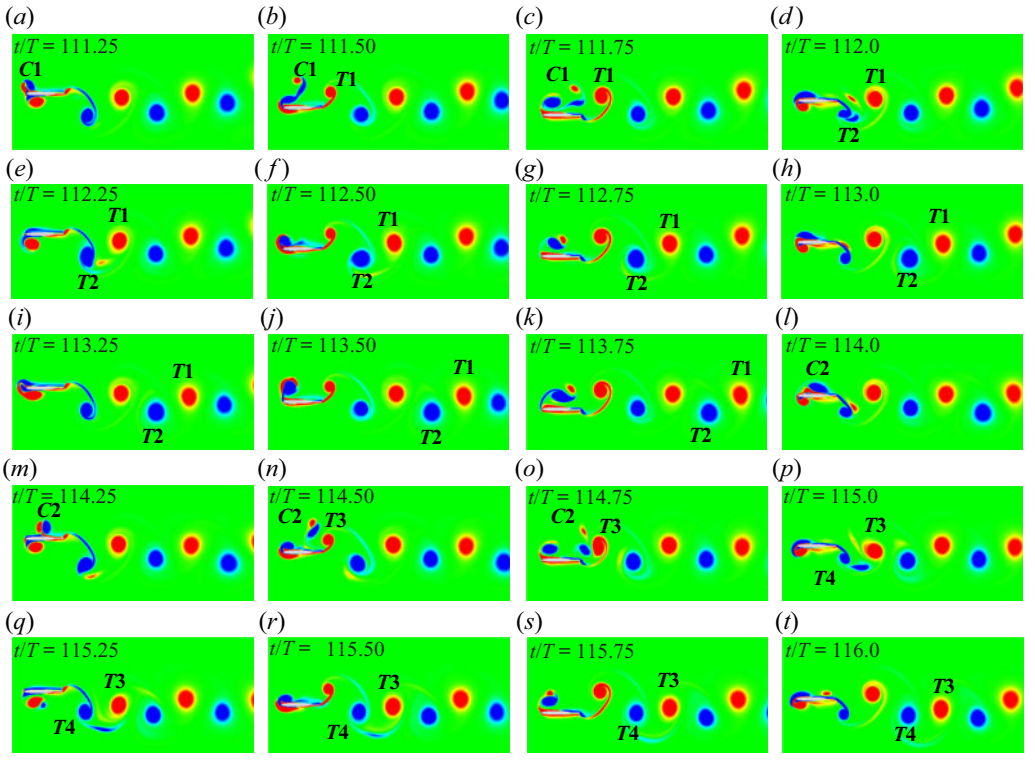

Figure 24. For $\kappa h = 1.5$, rigid tail: instantaneous vorticity contours during 112th to 116th cycles.

chaotic window B_1 is presented in figure 24. In the 112th cycle, leading-edge couple $\boldsymbol{C1}$ interacts with the nascent TEVs, $\boldsymbol{T1}$ and $\boldsymbol{T2}$, which were produced during consecutive half-strokes. Consequently, $\boldsymbol{T1}$ is not able to convect away but it stays close to $\boldsymbol{T2}$, which ensures a local dominance of downward deflecting couple $\boldsymbol{T2}$–$\boldsymbol{T1}$ (similar to couple $\boldsymbol{B}$–$\boldsymbol{C}$ of figure 13*b*). A similar set of events takes place during the 115th cycle as well, where $\boldsymbol{C2}$ influences the shedding of $\boldsymbol{T3}$ and $\boldsymbol{T4}$, resulting eventually in the dominance of downward deflecting $\boldsymbol{T4}$–$\boldsymbol{T3}$ (at $t/T = 116$ in figure 24*t*). Thus during the chaotic bursts in the intermittency regime, the primary LEV structures (say, $\boldsymbol{C1}$ or $\boldsymbol{C2}$) influence directly the shedding and convection of the TEVs (say, $\boldsymbol{T1}$ and $\boldsymbol{T2}$, or $\boldsymbol{T3}$ and $\boldsymbol{T4}$) through LEV–TEV interactions. This provides an additional impetus towards the formation of the symmetry-breaking couples, resulting in higher deflection angles and enhancement of the jet-switching process. Our previous studies (Majumdar *et al.* 2020*b*; Bose *et al.* 2021) and the present findings confirm that the LEV shedding and its subsequent interactions with the TEV are instrumental in the formation of the symmetry-breaking couples at the trailing edge, leading to vigorous jet-switching.

Note that the deflection angles reported in the present study, during the prominent jet-switching at $\kappa h = 1.5$, are smaller comparatively ($< 15^\circ$) than that reported in the experimental results of Heathcote & Gursul (2007*b*). This can be attributed possibly to the lower *Re* regime considered here, which is at least two orders of magnitude lower than that of the above-mentioned experimental study. Liang *et al.* (2011) and Zheng & Wei (2012) have shown that the wake deflection angle varies considerably with *Re*, and a decrease in *Re* results in a decrease in deflection angle as well. Besides, in the experiments with rigid

and flexible teardrop foils under quiescent flow, Heathcote & Gursul (2007*b*) observed the deflection angle to be higher than uniform inflow cases. Thus use of uniform free stream in the present simulations could also be another possible reason for encountering smaller angles compared to Heathcote & Gursul (2007*b*).

4. Effect of tail flexibility on the transitional dynamics

The flexible tail undergoes coupled fluid–structure interactions with the surrounding flow field, altering the features of LEV separation, TEV shedding, and LEV–TEV interactions. The flow-field behaviour triggering quasi-periodicity and intermittency gets changed, which affects eventually the formation of the dominant symmetry-breaking couples. These changes in the near field interfere with the jet-switching phenomenon and re-establish the symmetry in the wake. The underlying flow dynamics is examined in this section for $\kappa h = 1.5$ for two different flexibility levels of the aft-tail, referred to as flexibility levels I and II here. Recall that at this κh, a vigorous jet-switching associated with a dynamical state of intermittency was observed for the rigid tail configuration. It is observed here that the flexible deformation of the tail inhibits jet-switching for both flexibility levels I and II, which leads to quasi-periodic and periodic wake dynamics, respectively. This is in contrast to the state of intermittency observed for the rigid tail case. The underlying flow dynamics responsible for suppressing jet-switching and establishing symmetry in the wake are addressed in the following. To the best of the authors' knowledge, the role of flexibility behind the suppression of jet-switching with interlinked dynamical characteristics is being discussed for the first time in the present study.

4.1. *Flexibility level I: deflected wake pattern associated with quasi-periodic dynamics*

In contrast to the rigid tail configuration, the tail with flexibility level I ($\gamma = 0.1$) exhibits a downward deflected reverse Kármán street without any switching (figure 25*a*). In this case, the C_D time history reflects distinct quasi-periodic dynamics without any trace of intermittency (figure 26*a*). The corresponding reconstructed phase space depicts a well-developed toroidal portrait without any irregularities, which confirms the state to be pure quasi-periodic (figure 26*b*). The corresponding frequency spectrum is comprised of two incommensurate frequencies ($f_1 = 1.27$ and $f_2 = 0.87$), with other peaks being their linear combinations, which is again indicative of quasi-periodicity (figure 26*c*). The existence of these two incommensurate frequencies in the form of two narrow bands is also evident from the scalogram of the C_D time history in figure 26(*d*). Quasi-periodicity is also visible from the recurrence plot presented in figure 27, showing unequally spaced lines parallel to the main diagonal. To establish the presence of quasi-periodicity through a direct flow-field quantity, correlation coefficients $\rho(t)$ of the vorticity field are estimated. For details of the formulation of $\rho(t)$, please refer to our earlier study, Badrinath *et al.* (2017). The variation of the maximum $\rho(t)$ between 0.5 to 1 confirms the fact that the flow structures do not exactly repeat, nor are they completely different in consecutive cycles (figure 25*b*), which points to a quasi-periodic scenario. The details of the flow-field behaviour responsible for this change in the dynamics, in comparison to the rigid case, will be discussed in §§ 4.3 and 4.4.

4.2. *Flexibility level II: symmetric reverse Kármán wake with periodic dynamics*

As the flexibility increases to level II, the trailing wake shows a reverse Kármán street without any switching or even any strong deflection (figure 28*a*). Contrary to both the

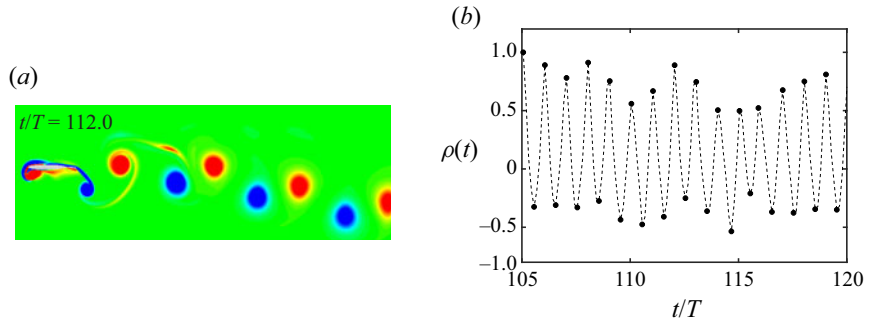

Figure 25. For $\kappa h = 1.5$, flexibility level I: (a) downward deflected vortex street, and (b) vorticity correlation.

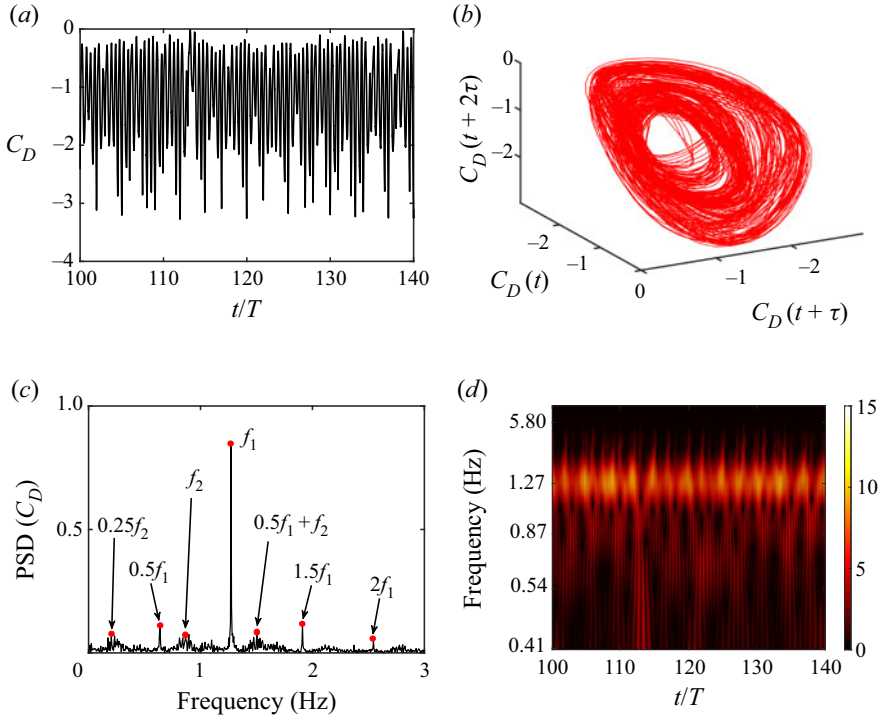

Figure 26. For $\kappa h = 1.5$, flexibility level I, time series analysis of C_D indicates quasi-periodic dynamics: (a) time history, (b) reconstructed phase portrait, (c) frequency spectra, and (d) wavelet transform.

cases of rigid and flexibility level I, the flow-field aperiodicity disappears in level II, and the wake vortices repeat almost exactly in consecutive cycles. Detailed flow-field comparisons are presented in §§ 4.3 and 4.4. The corresponding C_D time history has no modulations in its amplitude (figure 29a), and instead of a toroidal shape, two distinct closed loops in the reconstructed phase space are seen. The latter represent a period-2 signature; see figure 29(b). The frequency spectra (figure 29c) and the wavelet spectra (figure 29d) highlight a dominant frequency peak along with the subharmonics and superharmonics only. The uniformly spaced continuous lines parallel to the main diagonal in the recurrence plot as shown in figure 30 are characteristic of a periodic signal too.

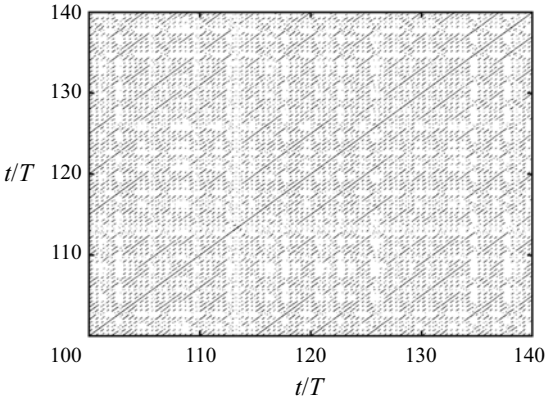

Figure 27. For $\kappa h = 1.5$, flexibility level I: recurrence plot of C_D.

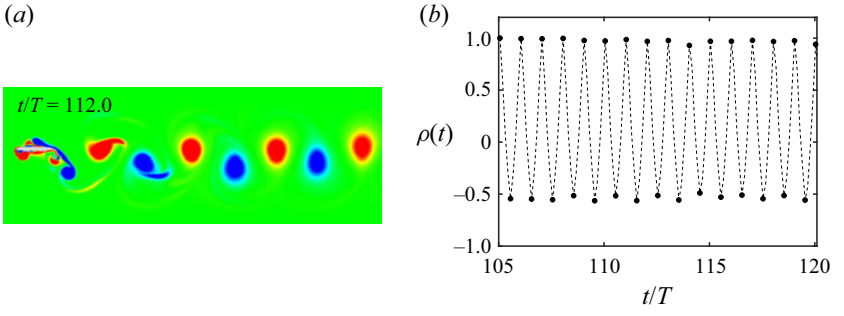

Figure 28. For $\kappa h = 1.5$, flexibility level II: (*a*) mildly deflected wake, and (*b*) vorticity correlation.

Also, the maximum correlation coefficient (ρ) of the vorticity field remains unity, which establishes the periodicity of the flow field (figure 28*b*).

4.3. *Difference in the wake deflection characteristics between the rigid and flexible configurations*

It is evident that the flow topology as well as the dynamical states undergoes a significant change as flexibility is introduced in the system, and as the flexibility increases, the trailing wake becomes more organised. The vigorous jet-switching at $\kappa h = 1.5$ seen for the rigid configuration is suppressed completely, and the trailing wake returns to a periodic reverse Kármán street at the higher flexibility level.

The instantaneous vorticity and velocity magnitude contours depicting the deflection angles of the jet at a few chosen cycles corresponding to the rigid and flexible tail configurations are compared in figure 31. The continuous temporal evolution of the flow fields for the respective cases are presented in supplementary movies 1, 2 and 3. Here, vigorous jet-switching with high deflection angles is observed for the rigid case. A downward deflected wake with $\Theta = -2.6$ is seen at $t/T = 104.0$, the deflection direction changes with time and the shed vortices start to move upwards, giving an upward deflected wake with $\Theta = 4.2$ at $t/T = 110.0$ (figures 31*a–d*). Such switchings between downward and upward directions continue to take place for the rigid case (see at $t/T = 119.0$ with $\Theta = -6.6$, and at $t/T = 126.0$ with $\Theta = 3.4$) . However, this gets inhibited with the

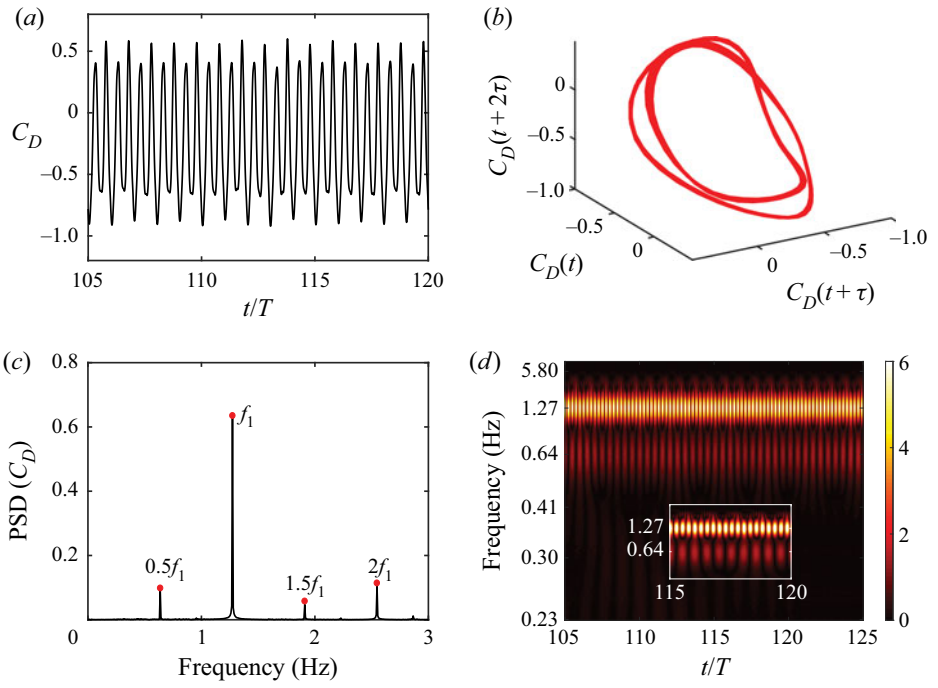

Figure 29. For $\kappa h = 1.5$, flexibility level II, time series analysis of C_D indicates periodic dynamics: (*a*) time history, (*b*) reconstructed phase portrait, (*c*) frequency spectra, and (*d*) wavelet transform.

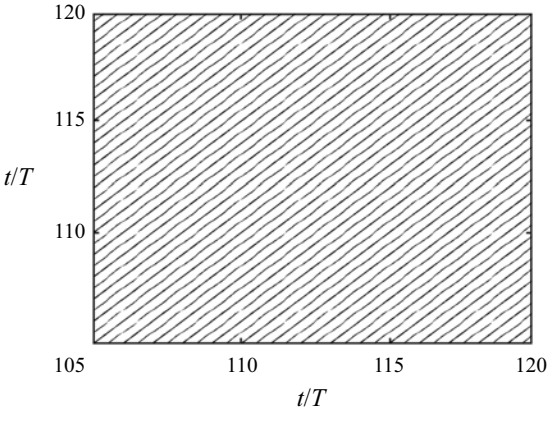

Figure 30. For $\kappa h = 1.5$, flexibility level II: recurrence plot of C_D.

introduction of flexibility, and at flexibility level I, the wake deflection direction no longer switches. It remains downward deflected for all time, with small time-dependent changes in its deflection angle (see figures 31*e–h*). With flexibility increasing to level II, the wake gets more regularised. It reorganises into a periodic reverse Kármán pattern with a very small deflection angle (figures 31*i–l*). The jet-switching and its inhibition at different flexibility levels reflect directly on the aerodynamic loads as well. This has been presented in terms of period-average lift coefficient in § 3 of the supplementary material.

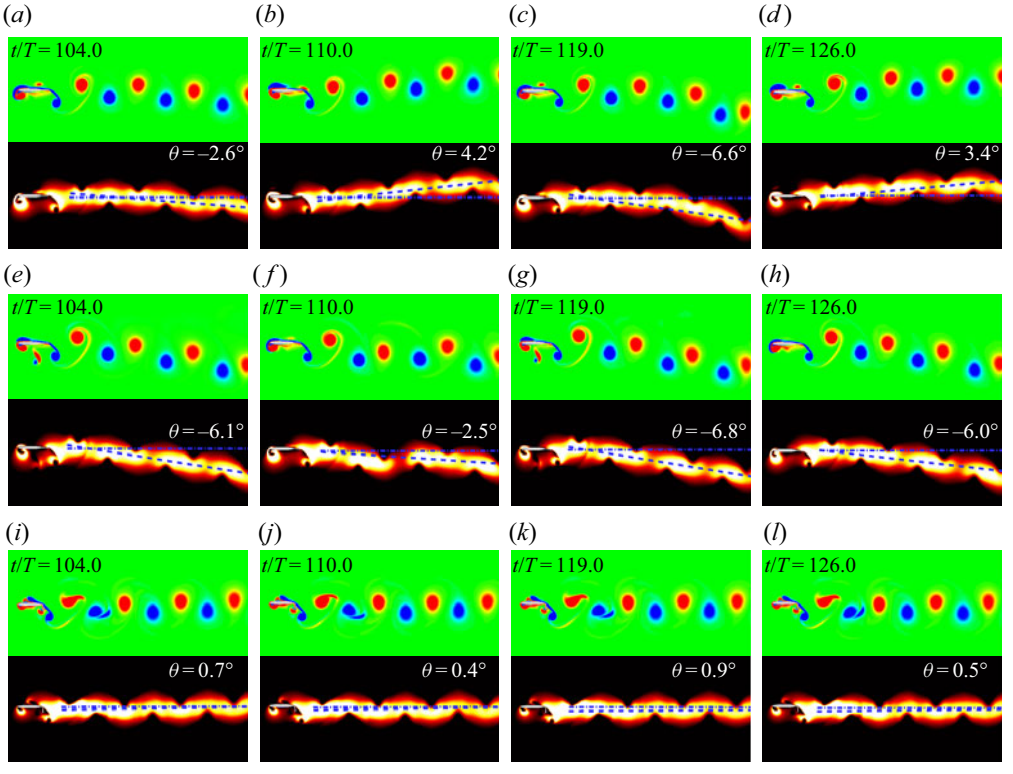

Figure 31. For $\kappa h = 1.5$, comparison of instantaneous vorticity fields and corresponding velocity magnitude contours for (*a–d*) rigid tail, (*e–h*) flexibility level I, and (*i–l*) flexibility level II.

The flip in the relative dominance of the upward and downward deflecting couples is responsible for the manifestation of jet-switching, and the ξ-ratio is the primary factor dictating the dominance of the symmetry-breaking couples (Majumdar *et al.* 2020*b*). Three representative cycles, at $t/T = 108$, 116, 126, are chosen to compare the ξ-ratios for rigid and flexible configurations in figure 32. The complete time evolution of the ξ-ratio is presented later, in figure 33(*c*). For the rigid tail, the ξ-ratio of ***A–B*** to ***B–C*** is seen to be less than unity ($\xi_{AB}/\xi_{BC} = 0.82$) at $t/T = 108$. Hence ***A–B*** forms the dominant couple, and this induces an upward jet that maintains the upward deflected wake subsequently (figures 32*a*,*d*,*g*). However, at $t/T = 116.0$, the ξ-ratio becomes 1.24, and the dominance is transferred to ***B–C***, which induces a downward jet causing the subsequently shed vortices to follow a downward deflected path (see at $t/T = 116.0$ in figures 32*a*,*d*,*g*). At $t/T = 126.0$, the ξ-ratio again becomes less than 1, indicating the dominance of upward deflecting ***A–B*** that gives way to another switching. The same was confirmed from the velocity magnitude contour plots in figures 31(*a–d*) as well.

The corresponding ξ-ratio for flexibility level I remains more than unity at all times with a varying magnitude, causing the wake to remain downward deflected, with the angle of deflection varying with time (figures 32*b*,*e*,*h*). Since the ξ-ratio remains always greater than 1, ***B–C*** is able to maintain its continuous dominance to pull the wake downwards at every cycle; see figures 32(*b*,*e*,*h*). As an outcome, the phenomenon of jet-switching gets suppressed. At flexibility level II, the ξ-ratio remains almost constant and quite close to unity (≈ 0.9), facilitating the upward

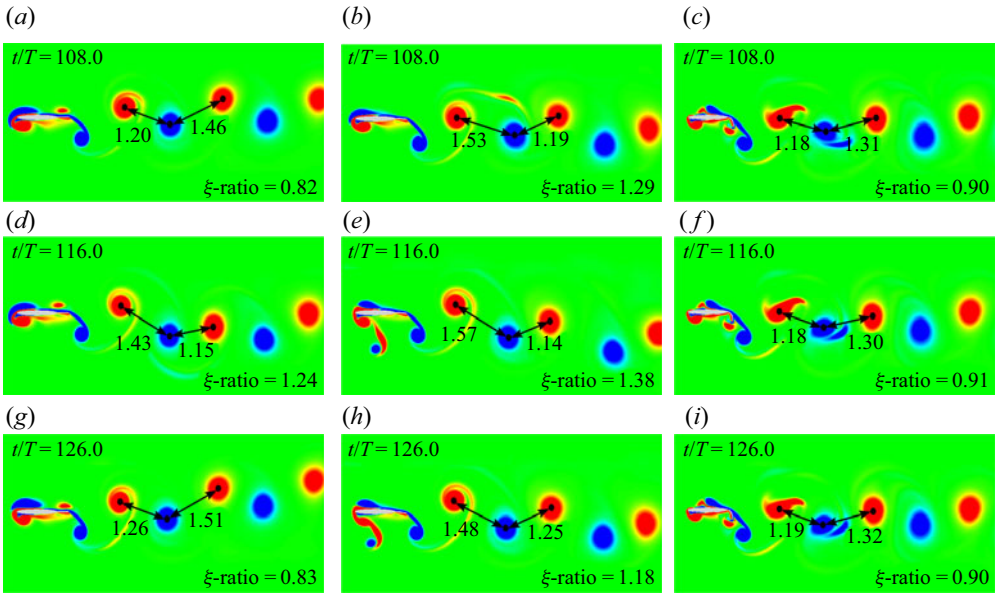

Figure 32. For $\kappa h = 1.5$, comparison of trailing-wake patterns showing the $\xi-$ratio for (a,d,g) rigid tail, (b,e,h) flexibility level I, and (c,f,i) flexibility level II.

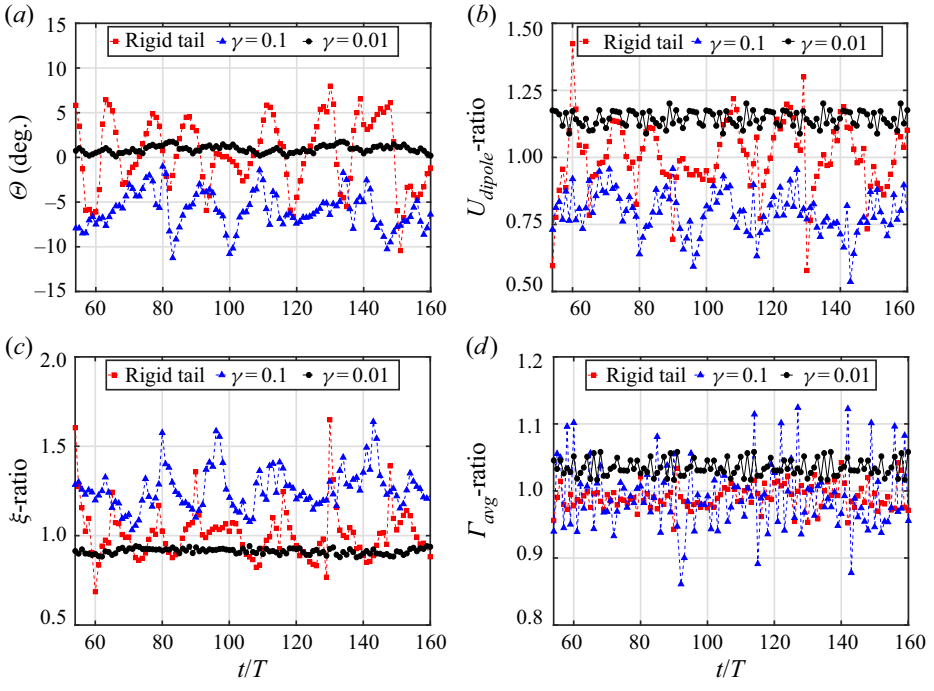

Figure 33. For $\kappa h = 1.5$, variation of: (a) deflection angle, (b) dipole velocity ratio, (c) distance ratio, and (d) average circulation ratio, for different aft-tail configurations.

deflecting couple ***A–B*** to maintain a small dominance forever. This results in an almost symmetric (with a negligible upward deflection) stable reverse Kármán street, as shown in figures 32(c,f,i).

The results can also be visualised quantitatively through a comparison of the time histories of different measures, as shown in figure 33. For the rigid tail, Θ crosses the zero mark multiple times, indicating multiple switchings; see figure 33(*a*). For flexibility level I, Θ varies with time but never changes its sign; hence jet-switching is absent and the wake stays downward deflected for all time. For flexibility level II, Θ remains nearly constant with time with a very small positive value close to zero, representative of a vortex street having a mild upward deflection. The temporal evolution of U_{dipole}-ratio, ξ-ratio and Γ_{avg}-ratio are shown in figures 33(*b*), 33(*c*) and 33(*d*), respectively. The ξ-ratio, and therefore the U_{dipole}-ratio, undergoes significant modulations around unity for the rigid case, leading to frequent shifts in the dominance of the symmetry-breaking couples that get manifested as vigorous switching. Note that the variation of the Γ_{avg}-ratio is relatively lesser, signifying its unimportant role in jet-switching. For flexibility level I, the fluctuations in ξ-ratio and U_{dipole}-ratio are seen to stay always above and below unity, respectively, as no change takes place in the deflection direction. With the increase in flexibility to level II, the fluctuations in these measures come down significantly as the wake gets reorganised into an almost symmetric reverse Kármán pattern.

4.4. *Underlying vortex interaction mechanisms*

From the above results, flexibility emerges as a crucial system parameter that can be manipulated to alter the dynamics as well as suppress the phenomenon of jet-switching. The near-field vortex interactions that lead to this suppression are examined in this subsection. It is important to understand the mechanism of change in the dominance and formation of the symmetry-breaking couples under the flexible tail configurations. In this regard, the chronology of vortex interactions during a typical flapping cycle is presented for flexibility levels I and II in figure 34. For flexibility level I, LEV $\boldsymbol{L1}^*$ initially sheds as a couple having a strong CCW and a fragile CW component at the start of the upstroke (see at $t/T = 110.125$ in figure 34*a*). Subsequently, the weaker CW component gets convected away, and the stronger CCW counterpart reattaches on the lower surface around the mid-chord, and gives rise to couple $\boldsymbol{C1}^*$ (see at $t/T = 110.375$ in figure 34*a*). In the next half-cycle, $\boldsymbol{C1}^*$ is shed from the lower surface and interacts with the CW TEV $\boldsymbol{T1}^*$, forming eventually a dominant downward deflected symmetry-breaking couple. The CW LEV $\boldsymbol{L2}^*$ does not shed from the foil (see $t/T = 110.625$ to 110.75 in figure 34*b*), but remains attached to the upper surface near the leading-edge and gets flattened gradually over the body ($t/T = 110.875$ to 111.0 in figure 34*b*). Note that $\boldsymbol{L2}^*$ does not participate in any interactions with the TEV. Therefore, the LEV–TEV interaction takes place asymmetrically and only at the lower surface of the foil. The asymmetric LEV–TEV interactions prevent a full reversal of the deflection direction, as only a downward deflected symmetry-breaking couple forms at every cycle. As the associated dynamical state is quasi-periodic, the strength of this couple varies from one cycle to another, resulting in a time-varying Θ behaviour (figure 33*a*).

As the flexibility increases to level II, the flow becomes more regularised, and the vortex interactions become symmetric between the upper and lower surfaces. Unlike level I, in this case an isolated CCW LEV, $\boldsymbol{L1}^*{*}$, is formed, which stays close to the lower surface of the foil. However, similar to flexibility level I, $\boldsymbol{L1}^*{*}$ forms couple $\boldsymbol{C1}^*{*}$ with a shear layer vortex while convecting towards the trailing edge. The strength of $\boldsymbol{C1}^*{*}$ is considerably lower than that of $\boldsymbol{C1}^*$ in the level I case, and it remains very close to the surface while moving downstream. Subsequently, $\boldsymbol{C1}^*{*}$ interacts with the highly deformed tail structure and gets trapped near it, preventing the couple from interacting directly with

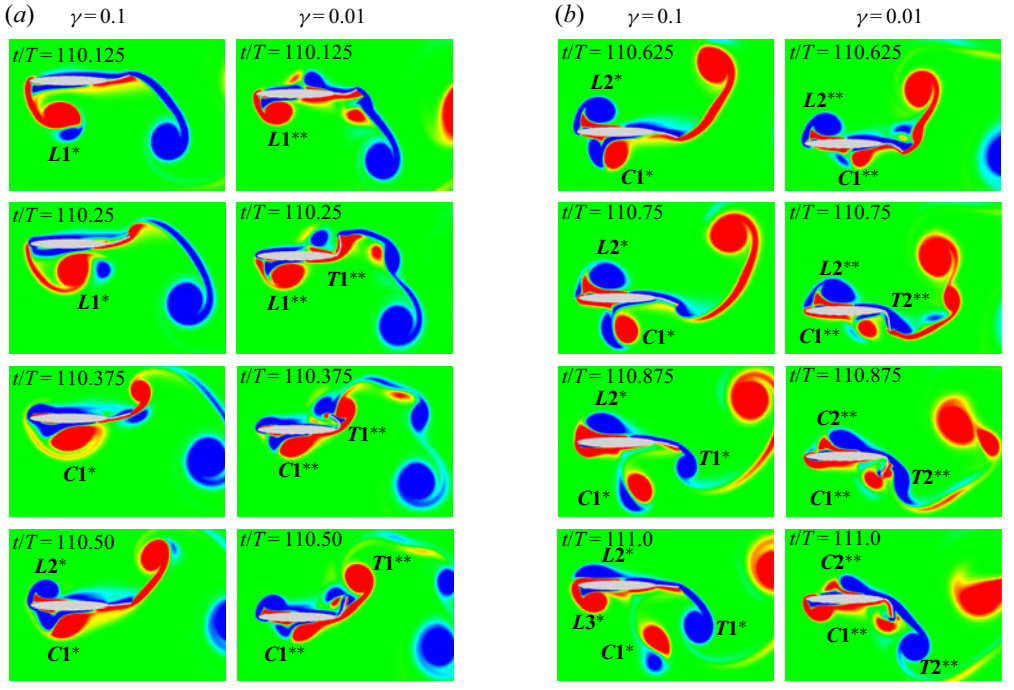

Figure 34. For $\kappa h = 1.5$, comparison of near-field vortex interactions at the 111th cycle: (*a*) first half-cycle, (*b*) second half-cycle; each left-hand column shows flexibility level I, and each right-hand column shows flexibility level II.

the TEV $\boldsymbol{T2}^{*}*$. Similar events occur on the upper surface in the following half-cycle as well, where LEV $\boldsymbol{L2}^{*}*$ forms couple $\boldsymbol{C2}^{*}*$. Similar to $\boldsymbol{C1}^{*}*$, $\boldsymbol{C2}^{*}*$ also does not get a chance to interact with the TEV due to its interaction with the highly deformed tail. The large bending of the flexible aft-tail inhibits the LEVs from interacting with the shed TEVs directly, thus preventing the formation of the symmetry-breaking couples that are the main agencies behind jet-switching. As a result, the near-wake vortices get well organised and finally settle into a near symmetric reverse Kármán wake through the merging of the same-signed vortices.

4.5. *Flexible deformation of the aft-tail leading to suppression of jet-switching*

Deformation of the flexible tail alters the interactions of the near-field vortices that decides the fate of the overall far-wake pattern. The deflection envelope and the phase plot of the tail-tip are shown in figure 35. The flexible tail acts as an inextensible cantilever beam clamped at the trailing edge of the foil. At flexibility level I, the tail is seen to bend predominantly in its first mode shape, as presented in figure 35(*a*). At flexibility level II, it exhibits mixed-mode oscillations involving both first and second modes with a significantly higher amplitude (figure 35*c*). In both these cases, the tip of the tail exhibits a 'figure-of-eight' motion (figures 35*b*,*d*). The phase portrait corresponding to level I in figure 35(*b*) is clearly indicative of a quasi-periodic dynamics, and this is triggered by the structure's coupled interactions with the quasi-periodic flow dynamics (presented in § 4.1). The flexibility level II case shows two distinct loops, representative of a period-2 dynamics (§ 4.2). Note that the flexible bending of the tail is influenced primarily by

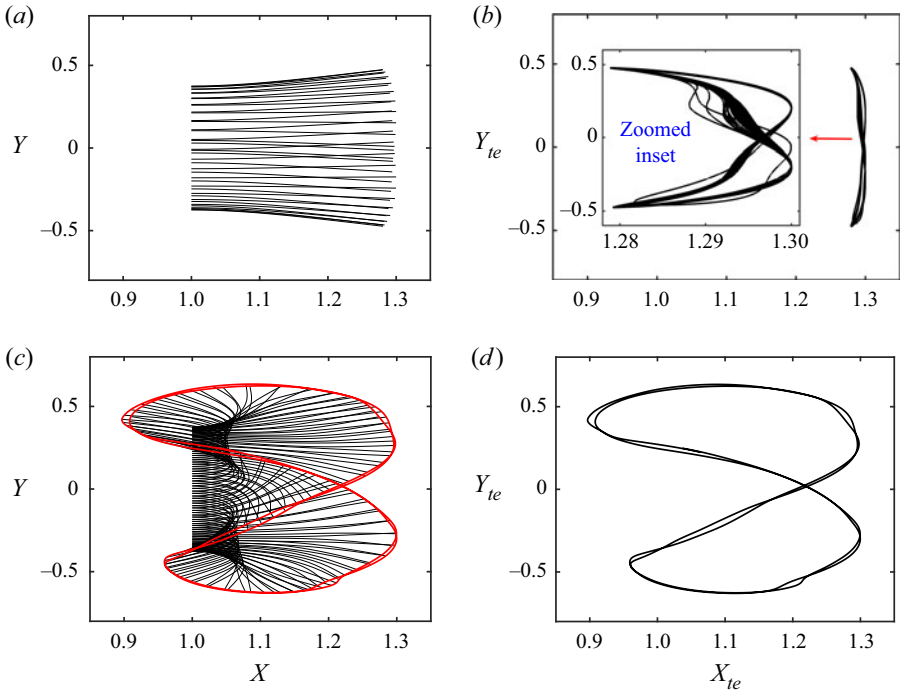

Figure 35. For $\kappa h = 1.5$, deflection envelopes and phase portraits for the tip displacement of the flexible tail for flexibility level I (*a*,*b*) and flexibility level II (*c*,*d*). (*a*) Mode shape structure for flexibility level I. (*b*) Phase plot of the free end of the trailing edge for flexibility level I. (*c*) Mode shape structure for flexibility level II. (*d*) Phase plot of the free end of the trailing edge for flexibility level II.

the trailing-edge separation in both the cases. However, the mild bending seen for level I does not prevent the LEV and the secondary vortices from interacting with the TEV. This gives way to the formation of the primary symmetry-breaking couple. At level II, the tail bends severely and even goes in the backward direction, taking an arch-like shape at the extreme positions. This highly deformed shape traps the LEVs and prevents the LEV–TEV interactions. Therefore, the resulting wake shape is dictated by the shedding of the strong TEVs, and the spatial symmetry of the wake is more or less retained.

The pressure coefficient (C_P) contours are compared in figure 36 for the three different tail configurations at the end of upstroke and downstroke of a typical cycle ($t/T = 110.25$ and 110.75, respectively). For the rigid tail case, a large low-pressure zone is seen to be present near the leading edge. This is followed by a high-pressure zone extended up to the trailing end of the tail along the lower surface, at the beginning of the upstroke. This creates a strong adverse pressure gradient. Also, a reverse flow is observed close to the leading edge; see figure 36(*a*), where the velocity field is marked by the arrows. A strong CCW LEV (***L2***) gets shed due to the strong adverse pressure gradient, and, it interacts with the TEV subsequently to result in the formation of a symmetry-breaking couple. A similar strong low-pressure zone followed by a high-pressure zone on the upper surface of the foil is observed during the end of the downstroke (see figure 36*d*). Therefore, separation of the LEVs (***L2*** and ***L10***, corresponding to figure 23) takes place from both upper and lower surfaces. This in turn results in the formation of upward and downward deflected symmetry-breaking couples. As discussed in the previous subsection, these symmetry-breaking couples are responsible for triggering jet-switching in case of

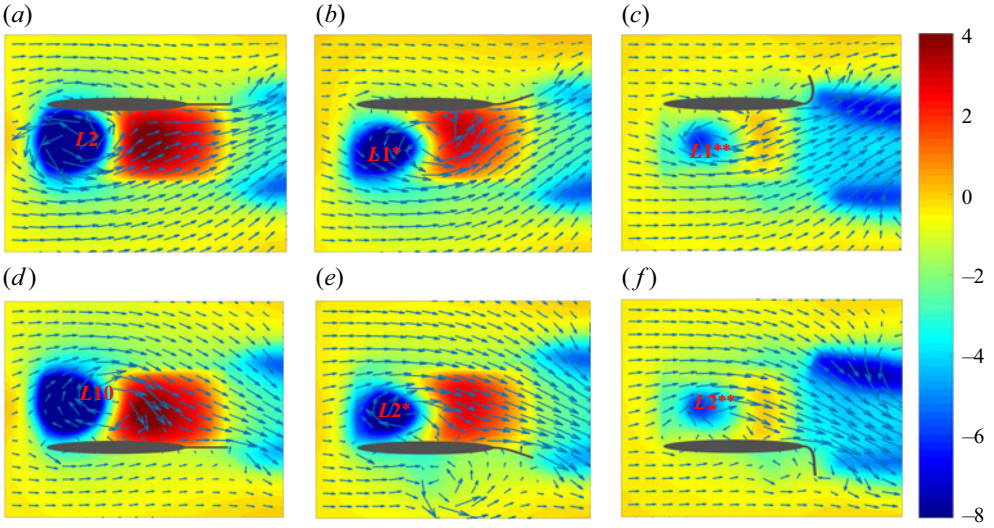

Figure 36. For $\kappa h = 1.5$, comparison of pressure coefficient (C_P) contours during the end of (*a–c*) upstroke ($t/T = 110.25$) and (*d–f*) downstroke ($t/T = 110.75$), for (*a*,*d*) rigid tail, (*b*,*e*) flexibility level I, and (*c*,*f*) flexibility level II. Lengths of arrows indicate the magnitude of the velocity vector field.

the rigid configuration. In contrast, for flexibility level I, separation of the CCW LEV ($\boldsymbol{L1}^*$) takes place only during the upstroke. Due to a high adverse pressure gradient, counter-clockwise LEVs are formed and separated at the lower surface during the upstroke. But the flow on the upper surface remains smooth, as indicated by the unidirectional vector field (figure 36(*b*) at $t/T = 110.25$). During the downstroke, a reverse flow is observed along both the surfaces, and the CW LEV ($\boldsymbol{L2}^*$) in the upper surface does not get separated but circumnavigates the leading edge to traverse in the lower surface. So LEV–TEV interaction occurs only along the lower surface in every cycle. Hence the trailing wake remains deflected in the same direction always – though, depending on the strengths of the LEV and the TEV, the magnitude of the deflection angle changes as was presented in § 4.1. For level II, the low- and high-pressure zones get reduced significantly due to the severe deformation of the tail; see figures 36(*c*,*f*). Furthermore, the downstream low-pressure zone comes much closer to the foil, increasing the suction. This pulls the upstream fluid at a faster rate as indicated by the longer lengths of the arrows. Therefore, the LEVs ($\boldsymbol{L1}^*{*}$ and $\boldsymbol{L2}^*{*}$) do not get sufficient time to grow and separate. Instead, the LEVs stay close to the body, roll over the surface, and get trapped eventually in the vicinity of the flexible tail. No shedding of them happens during the upstroke or the downstroke. The flow remains almost periodic, without the formation of any symmetry-breaking couples, thereby inhibiting the jet-switching process.

4.6. *Effect of the aft-tail length (L_t) on the flow-field dynamics*

The results presented so far have been able to identify tail flexibility as a potential instrument for inhibiting jet-switching, by following the flow-field interactions systematically and interlinking them with the associated nonlinear dynamical states. In the earlier subsections, interactions of the near-field vortices have been investigated, and the corresponding nonlinear dynamical states were established using different qualitative and

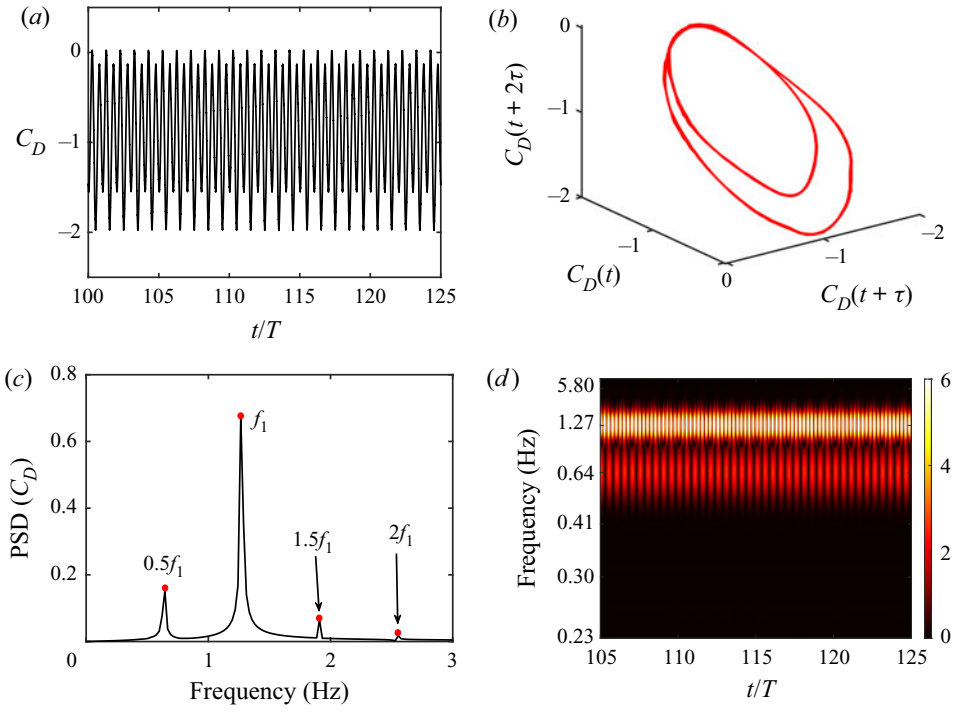

Figure 37. Changed tail length: $\kappa h = 1.5$, $\gamma = 0.1$, aft-tail length $L_t = 0.38c$. Time series analysis of C_D indicates periodic dynamics: (*a*) time history, (*b*) reconstructed phase portrait, (*c*) frequency spectra, and (*d*) wavelet transform.

quantitative flow-field measures, and time series tools. The flow mechanisms of flexibility influencing directly the formation of symmetry-breaking couples, which dictate the wake deflection characteristics and play a pivotal role in triggering jet-switching (Godoy-Diana *et al.* 2009; Zheng & Wei 2012; Majumdar *et al.* 2020*b*), were also highlighted. It is worth noting that in the previous subsections, the length of the flexible tail was kept constant, and the non-dimensional bending rigidity has been varied to increase the flexibility. However, one can change the degree of flexibility by changing the aft-tail length as well, keeping the non-dimensional bending rigidity fixed (which is not a function of the length in any implicit manner). The effect of aft-tail length on the wake dynamics is not clear from the existing literature and is of interest to the present subsection. The present results obtained so far in this direction indicate that the tail length, being another crucial parameter to govern the flexibility level of the system, can play an important role in regularising a non-periodic wake. Therefore, both the non-dimensional bending rigidity and the aft-tail length can be considered as alternative choices for benefiting the design of engineering devices, ensuring a periodic wake to maximise the aerodynamic efficiency.

Here, results are presented for a typical case of aft-tail length of $L_t = 0.38c$, for $\gamma = 0.1$ and $\kappa h = 1.5$. As was shown in § 4.1, the wake deflected downwards with quasi-periodic dynamics for $L_t = 0.3c$. But as L_t is increased to $0.38c$, the wake turns periodic, as can be confirmed by the C_D time history shown in figure 37(*a*), which represents a completely periodic response with no amplitude modulation. The closed loop in the corresponding reconstructed phase space, dominant frequency peak with subharmonics and superharmonics in the frequency spectra, and narrow bands of harmonic frequencies

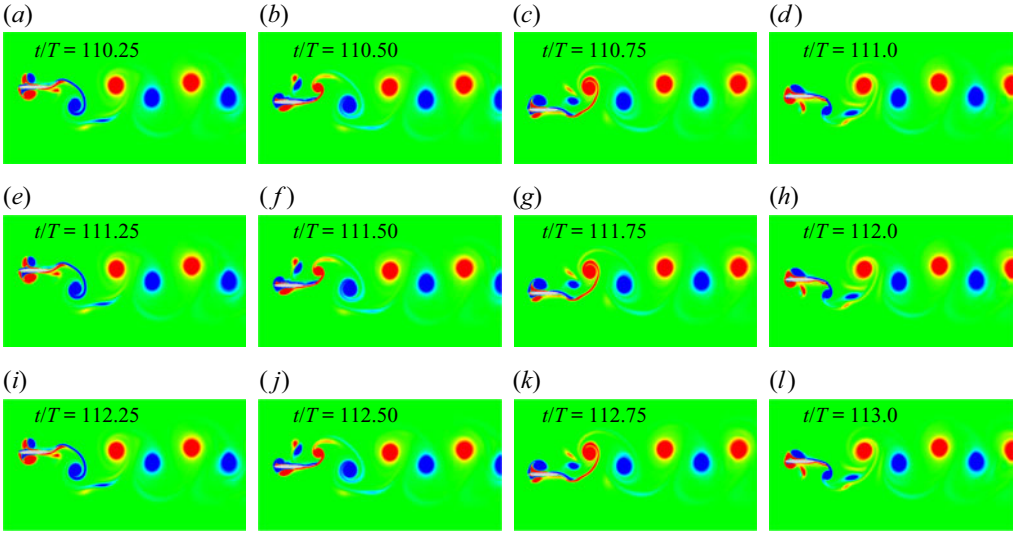

Figure 38. Changed tail length: $\kappa h = 1.5$, $\gamma = 0.1$, aft-tail length $L_t = 0.38c$. Instantaneous vorticity contours during 111th–113th cycles.

in the wavelet spectra, further establish the periodic dynamics; see figures 37(*b*), 37(*c*) and 37(*d*), respectively. The instantaneous vorticity contours for three consecutive cycles (111th–113th) are presented in figure 38. The flow field is seen to be repeating exactly from one cycle to another, confirming the periodicity of the wake. In contrast to the tail length $L_t = 0.3c$, the vortices are regularised, and the wake can be characterised by a reverse Kármán street with very mild upward deflection ($\Theta = 1.65^\circ$) at $L_t = 0.38$; see figures 39(*a*,*b*). The periodic nature of the flow field is confirmed further quantitatively from the vorticity correlation plot where the maximum value of ρ reaches unity in every cycle; see figure 39(*c*). Here, Θ remains nearly constant with time, with a small positive value representative of the vortex street having a mild deflection (figure 40*a*). A slight dominance of upward deflecting couple ***A*–*B*** can be visualised through the temporal evolution of U_{dipole}-ratio, ξ-ratio and Γ_{avg}-ratio presented in figure 40(*b*). The ξ-ratio and U_{dipole}-ratio are always below and above unity, respectively, and remain constant in every cycle. Therefore, the couple ***A*–*B*** always remains dominant, resulting in a slightly upward-looking wake. The continuous temporal evolution of the flow field for the present case is presented in supplementary movie 4.

The deflection envelope and the corresponding phase plot of the tail-tip are presented in figure 41. The tail bends with a little asymmetry and shows mostly a first-mode oscillation profile. The mechanism by which the tail influences the near field can be understood better from the C_P contour during the end of upstroke and downstroke as shown in figure 42. The downstream low-pressure zone created by the deflection of the tail sucks the upstream fluid at a faster rate, as indicated by the longer lengths of the arrows. Hence the LEVs do not get sufficient time to grow and separate, instead getting trapped in the vicinity of the tail, similar to flexibility level II as was shown in § 4.5. The flow remains periodic without the formation of any symmetry-breaking couples, thereby inhibiting jet-switching and maintaining periodicity. This also evidently underlines the role of the length of the tail in influencing the dynamical transitions of the system. Therefore, an appropriate selection of the aft-tail length and bending rigidity inhibits the aperiodicity in the flow

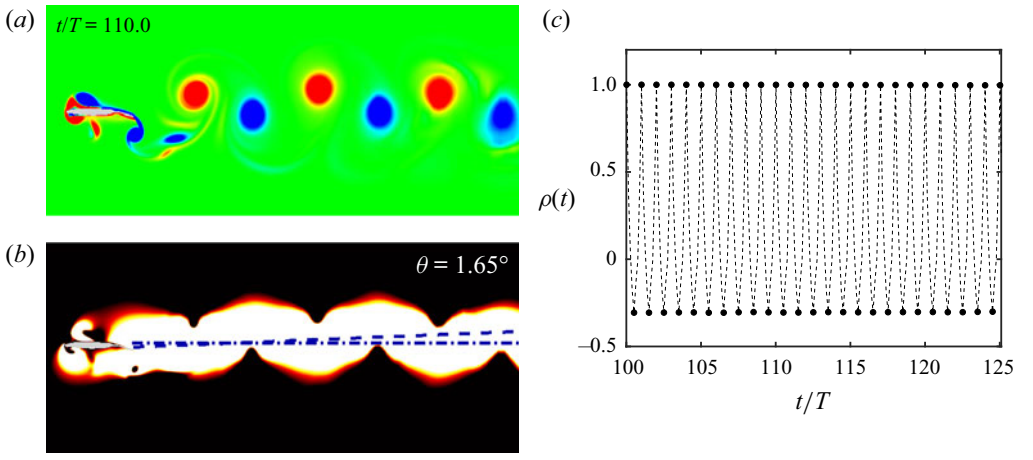

Figure 39. Changed tail length: $\kappa h = 1.5$, $\gamma = 0.1$, aft-tail length $L_t = 0.38c$. (*a*) Instantaneous vorticity and (*b*) velocity magnitude, contours depicting reverse Kármán wake with mild upward deflection; and (*c*) vorticity correlation.

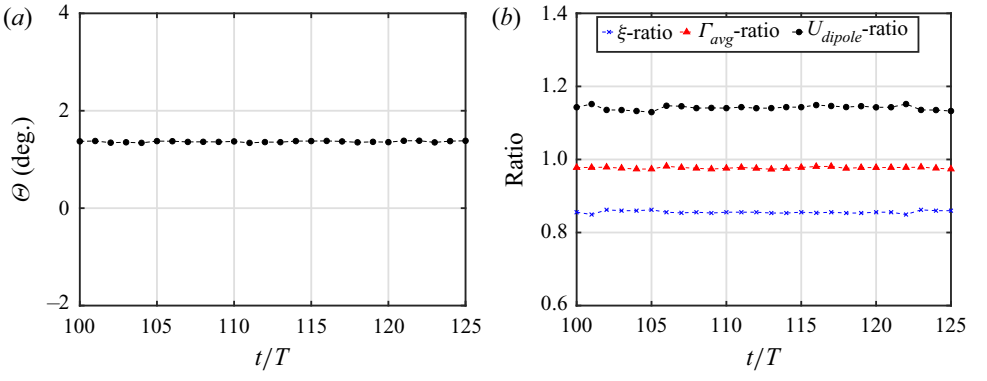

Figure 40. Changed tail length: $\kappa h = 1.5$, $\gamma = 0.1$, aft-tail length $L_t = 0.38c$. (*a*) Wake deflection angle and (*b*) quantitative measures associated with the vortex system. Dominant effect of the upward deflecting vortex couple ***A***–***B*** results in a positive deflection angle.

field. To the best of the authors' knowledge, the effect of aft-tail length in inhibiting the jet-switching and regularising the flow field has not yet been taken up adequately in the existing literature. Note that design of flapping devices based on natural flyers/swimmers would like to avoid aperiodicity to propel efficiently by exploiting the combination of the length of flapping appendages and the wing/fin morphology. The present results contribute towards that by adding insights on the role of flexibility in suppressing the switching and inhibiting aperiodicity in the wake. Currently, the authors are studying the effect of a flexible aft-tail in delaying the onset of aperiodicity at higher values of κh.

5. Conclusions

The present study analyses the role of tail flexibility in suppressing the jet-switching phenomenon in the wake of a heaving foil, and interlinks the underlying flow-field interaction mechanisms with the corresponding nonlinear dynamical signatures of the wake. With a fully rigid aft-tail, mild jet-switching is observed at $\kappa h = 1.2$, due to

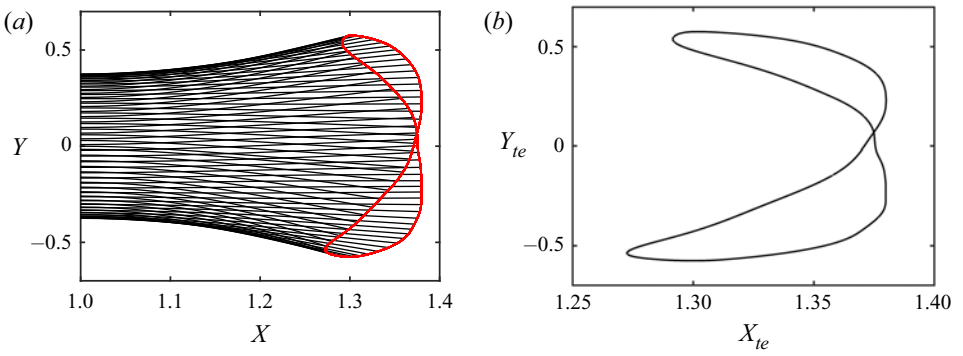

Figure 41. Changed tail length: $\kappa h = 1.5$, $\gamma = 0.1$, aft-tail length $L_t = 0.38c$, (*a*) Deflection envelopes, mode shape structure. (*b*) Phase plot of the tail-tip of the flexible tail.

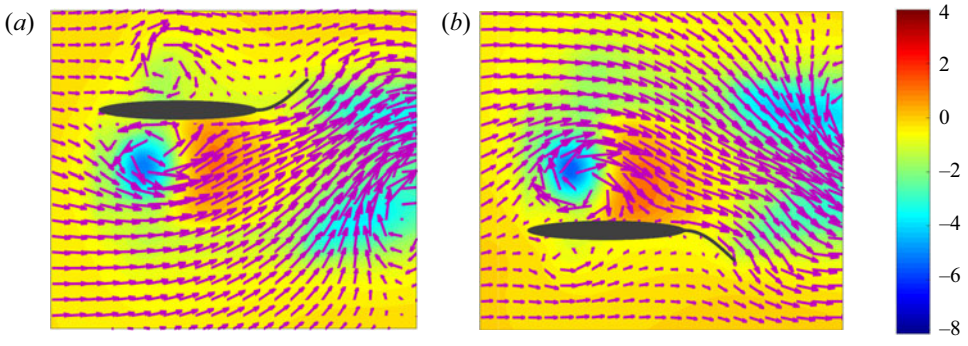

Figure 42. Changed tail length: $\kappa h = 1.5$, $\gamma = 0.1$, aft-tail length $L_t = 0.38c$. Pressure coefficient (C_P) contours during the end of (*a*) upstroke ($t/T = 110.25$), and (*b*) downstroke ($t/T = 110.75$).

quasi-periodic movement of the wake vortices. Vigorous and frequent jet-switching with large deflection is observed at $\kappa h = 1.5$, due to sporadic bursts of aperiodic interactions of near-field vortices, as the dynamics changes from quasi-periodicity to the state of intermittency. During the intermittent bursts, the primary LEV interacts directly with the TEV that gives way to the formation of strong symmetry-breaking couples, which trigger the switching phenomenon. The LEV–TEV interactions take place from both upper and lower surfaces of the body, thus forming alternate (upward and downward deflecting) symmetry-breaking couples.

Two different flexibility levels of the aft-tail have been considered in the present study. In the presence of flexibility, the intermittent dynamics and the associated vigorous jet-switching are suppressed through a regularisation of the flow field. At the lower flexibility level, a downward deflected reverse Kármán wake with varying deflection angle is observed. In this case, the flexible tail modifies the near field in such a way that the LEV–TEV interactions take place only along the lower surface in each cycle, thereby producing only one type of symmetry-breaking couple (downward deflecting). This makes the resulting wake stay deflected in the downward direction for all time. At the higher flexibility of the aft-tail, the flow field gets further regularised, and the wake settles into a periodic reverse Kármán street with a mild deflection. In this case, a highly deformed tail prevents LEV–TEV interactions completely by trapping the LEV structures within

its vicinity. This inhibits the formation of any strong symmetry-breaking couples, and as a result, jet-switching gets suppressed. Similar regularisation in the wake can be achieved by altering the aft-tail length. For higher aft-tail length at a moderate rigidity level, the wake was seen to settle into an almost perfect reverse Kármán street. Thus the regularisation of the non-periodic flow field can be achieved in both ways.

Supplementary material and movies. Supplementary material and movies are available at https://doi.org/10.1017/jfm.2022.591.

Declaration of interests. The authors report no conflict of interest.

Author ORCIDs.
Chhote Lal Shah https://orcid.org/0000-0002-1061-0916;
Dipanjan Majumdar https://orcid.org/0000-0002-3551-3768;
Chandan Bose https://orcid.org/0000-0001-5166-9968;
Sunetra Sarkar https://orcid.org/0000-0003-0331-0138.

References

ANDERSON, J.D. JR. 2010 *Fundamentals of Aerodynamics*. Tata McGraw-Hill Education.

ASHRAF, M.A., YOUNG, J. & LAI, J.C.S. 2012 Oscillation frequency and amplitude effects on plunging airfoil propulsion and flow periodicity. *AIAA J.* **50** (11), 2308–2324.

BADRINATH, S., BOSE, C. & SARKAR, S. 2017 Identifying the route to chaos in the flow past a flapping airfoil. *Eur. J. Mech. B/Fluids* **66**, 38–59.

BOSE, C., GUPTA, S. & SARKAR, S. 2021 Dynamic interlinking between near- and far-field wakes behind a pitching–heaving airfoil. *J. Fluid Mech.* **911**, A31.

BOSE, C. & SARKAR, S. 2018 Investigating chaotic wake dynamics past a flapping airfoil and the role of vortex interactions behind the chaotic transition. *Phys. Fluids* **30** (4), 047101.

CLEAVER, D.J., WANG, Z. & GURSUL, I. 2013 Investigation of high-lift mechanisms for a flat-plate airfoil undergoing small-amplitude plunging oscillations. *AIAA J.* **51** (4), 968–980.

COMBES, S.A. & DANIEL, T.L. 2003 Flexural stiffness in insect wings. II. Spatial distribution and dynamic wing bending. *J. Expl Biol.* **206** (17), 2989–2997.

DANIEL, T.L. & COMBES, S.A. 2002 Flexible wings and fins: bending by inertial or fluid-dynamic forces? *Integr. Compar. Biol.* **42** (5), 1044–1049.

DENG, J., SUN, L. & SHAO, X. 2015 Dynamical features of the wake behind a pitching foil. *Phys. Rev.* E **92** (6), 063013.

ENNOS, A.R. 1988 The importance of torsion in the design of insect wings. *J. Expl Biol.* **140** (1), 137–160.

GODOY-DIANA, R., AIDER, J.L. & WESFREID, J.E. 2008 Transitions in the wake of a flapping foil. *Phys. Rev.* E **77** (1), 016308.

GODOY-DIANA, R., MARAIS, C., AIDER, J.-L. & WESFREID, J.E. 2009 A model for the symmetry breaking of the reverse Bénard–von Kármán vortex street produced by a flapping foil. *J. Fluid Mech.* **622**, 23–32.

GURSUL, I. & CLEAVER, D. 2019 Plunging oscillations of airfoils and wings: progress, opportunities, and challenges. *AIAA J.* **57** (9), 3648–3665.

HEATHCOTE, S. & GURSUL, I. 2007*a* Flexible flapping airfoil propulsion at low Reynolds numbers. *AIAA J.* **45** (5), 1066–1079.

HEATHCOTE, S. & GURSUL, I. 2007*b* Jet switching phenomenon for a periodically plunging airfoil. *Phys. Fluids* **19** (2), 027104.

HEATHCOTE, S., WANG, Z. & GURSUL, I. 2008 Effect of spanwise flexibility on flapping wing propulsion. *J. Fluids Struct.* **24** (2), 183–199.

HILBORN, R.C., *et al.* 2000 *Chaos and Nonlinear Dynamics: An Introduction for Scientists and Engineers*. Oxford University Press.

HUANG, W.X., SHIN, S.J. & SUNG, H.J. 2007 Simulation of flexible filaments in a uniform flow by the immersed boundary method. *J. Comput. Phys.* **226** (2), 2206–2228.

JONES, K.D., DOHRING, C.M. & PLATZER, M.F. 1998 Experimental and computational investigation of the Knoller–Betz effect. *AIAA J.* **36** (7), 1240–1246.

KANG, C.K., AONO, H., CESNIK, C.E.S. & SHYY, W. 2011 Effects of flexibility on the aerodynamic performance of flapping wings. *J. Fluid Mech.* **689**, 32–74.

KIM, J., KIM, D. & CHOI, H. 2001 An immersed-boundary finite-volume method for simulations of flow in complex geometries. *J. Comput. Phys.* **171** (1), 132–150.
KOOCHESFAHANI, M.M. 1989 Vortical patterns in the wake of an oscillating airfoil. *AIAA J.* **27** (9), 1200–1205.
LAI, J.C.S. & PLATZER, M.F. 1999 Jet characteristics of a plunging airfoil. *AIAA J.* **37** (12), 1529–1537.
LEE, I. & CHOI, H. 2015 A discrete-forcing immersed boundary method for the fluid–structure interaction of an elastic slender body. *J. Comput. Phys.* **280**, 529–546.
LEE, J., KIM, J., CHOI, H. & YANG, K.-S. 2011 Sources of spurious force oscillations from an immersed boundary method for moving-body problems. *J. Comput. Phys.* **230** (7), 2677–2695.
LENTINK, D., VAN HEIJST, G.F., MUIJRES, F.T. & VAN LEEUWEN, J.L. 2010 Vortex interactions with flapping wings and fins can be unpredictable. *Biol. Lett.* **6** (3), 394–397.
LEWIN, G.C. & HAJ-HARIRI, H. 2003 Modelling thrust generation of a two-dimensional heaving airfoil in a viscous flow. *J. Fluid Mech.* **492**, 339–362.
LIANG, C., OU, K., PREMASUTHAN, S., JAMESON, A. & WANG, Z.J. 2011 High-order accurate simulations of unsteady flow past plunging and pitching airfoils. *Comput. Fluids* **40** (1), 236–248.
MAJUMDAR, D., BOSE, C. & SARKAR, S. 2020*a* Capturing the dynamical transitions in the flow-field of a flapping foil using immersed boundary method. *J. Fluids Struct.* **95**, 102999.
MAJUMDAR, D., BOSE, C. & SARKAR, S. 2020*b* Effect of gusty inflow on the jet-switching characteristics of a plunging foil. *Phys. Fluids* **32** (11), 117105.
MAJUMDAR, D., BOSE, C. & SARKAR, S. 2022 Transition boundaries and an order-to-chaos map for the flow field past a flapping foil. *J. Fluid Mech.* **942**, A40.
MARAIS, C., THIRIA, B., WESFREID, J.E. & GODOY-DIANA, R. 2012 Stabilizing effect of flexibility in the wake of a flapping foil. *J. Fluid Mech.* **710**, 659–669.
MAZAHERI, K. & EBRAHIMI, A. 2010 Experimental investigation of the effect of chordwise flexibility on the aerodynamics of flapping wings in hovering flight. *J. Fluids Struct.* **26** (4), 544–558.
RAMANANARIVO, S., GODOY-DIANA, R. & THIRIA, B. 2011 Rather than resonance, flapping wing flyers may play on aerodynamics to improve performance. *Proc. Natl Acad. Sci. USA* **108** (15), 5964–5969.
SCHNIPPER, T., ANDERSEN, A. & BOHR, T. 2009 Vortex wakes of a flapping foil. *J. Fluid Mech.* **633**, 411–423.
SHAH, C.L., MAJUMDAR, D. & SARKAR, S. 2019 Performance enhancement of an immersed boundary method based FSI solver using OpenMP. In *21st Annual CFD Symposium. NAL, Bangalore, India*.
SHINDE, S.Y. & ARAKERI, J.H. 2013 Jet meandering by a foil pitching in quiescent fluid. *Phys. Fluids* **25** (4), 041701.
SHINDE, S.Y. & ARAKERI, J.H. 2014 Flexibility in flapping foil suppresses meandering of induced jet in absence of free stream. *J. Fluid Mech.* **757**, 231–250.
SHYY, W., AONO, H., CHIMAKURTHI, S.K., TRIZILA, P., KANG, C.-K., CESNIK, C.E.S. & LIU, H. 2010 Recent progress in flapping wing aerodynamics and aeroelasticity. *Prog. Aerosp. Sci.* **46** (7), 284–327.
SHYY, W., BERG, M. & LJUNGQVIST, D. 1999 Flapping and flexible wings for biological and micro air vehicles. *Prog. Aerosp. Sci.* **35** (5), 455–505.
SUN, L., DENG, J. & SHAO, X. 2018 Three-dimensional instabilities for the flow around a heaving foil. *Phys. Rev.* E **97** (1), 013110.
TRIANTAFYLLOU, M.S., TECHET, A.H. & HOVER, F.S. 2004 Review of experimental work in biomimetic foils. *IEEE J. Ocean. Engng* **29** (3), 585–594.
TRIANTAFYLLOU, M.S., TRIANTAFYLLOU, G.S. & YUE, D.K.P. 2000 Hydrodynamics of fishlike swimming. *Annu. Rev. Fluid Mech.* **32** (1), 33–53.
VANELLA, M., FITZGERALD, T., PREIDIKMAN, S., BALARAS, E. & BALACHANDRAN, B. 2009 Influence of flexibility on the aerodynamic performance of a hovering wing. *J. Expl Biol.* **212** (1), 95–105.
VISBAL, M.R. 2009 High-fidelity simulation of transitional flows past a plunging airfoil. *AIAA J.* **47** (11), 2685–2697.
WEI, Z. & ZHENG, Z.C. 2014 Mechanisms of wake deflection angle change behind a heaving airfoil. *J. Fluids Struct.* **48**, 1–13.
WOOTTON, R.J. 1999 Invertebrate paraxial locomotory appendages: design, deformation and control. *J. Expl Biol.* **202** (23), 3333–3345.
WU, J., WU, J., TIAN, F.B., ZHAO, N. & LI, Y.D. 2015 How a flexible tail improves the power extraction efficiency of a semi-activated flapping foil system: a numerical study. *J. Fluids Struct.* **54**, 886–899.
ZHENG, Z.C. & WEI, Z. 2012 Study of mechanisms and factors that influence the formation of vortical wake of a heaving airfoil. *Phys. Fluids* **24** (10), 103601.
ZHU, X., HE, G. & ZHANG, X. 2014 Numerical study on hydrodynamic effect of flexibility in a self-propelled plunging foil. *Comput. Fluids* **97**, 1–20.